JOURNAL OF PETROLOGY | VOLUME 51 | NUMBER 11 | PAGES 2211–2243 | 2010 | doi:10.1093/petrology/egq054

High-pressure Hydrous Phase Relations of Radiolarian Clay and Implications for the Involvement of Subducted Sediment in Arc Magmatism

SUSANNE SKORA* AND JON BLUNDY

DEPARTMENT OF EARTH SCIENCES, UNIVERSITY OF BRISTOL, WILLS MEMORIAL BUILDING, BRISTOL BS8 1RJ, UK

RECEIVED JANUARY 19, 2010; ACCEPTED AUGUST 24, 2010
ADVANCE ACCESS PUBLICATION OCTOBER 1, 2010

Melting of subducted oceanic sediment is considered to play a key role in the generation of the arc magmatic signature. We have carried out an experimental study on hydrous melting of trace element-doped radiolarian clay at 3 GPa and temperatures from 700 to 1250°C; 7–15 wt % H_2O was added to the sediment to simulate the effects of flushing by fluids derived from underlying dehydrating lithologies, such as serpentinites. Melting begins at ~750°C owing to the breakdown of phengite + clinopyroxene + coesite and a hydrous melt coexists with mostly garnet + kyanite ± quartz up to around 1250°C. Rutile and Fe–Ti oxides are present to ~1000°C. Very high degrees of melting occur at relatively low, supra-solidus temperatures (e.g. with 15 wt % added H_2O, the clay is ~54% molten at 800°C), in marked contrast to fluid-absent melting of similar rock compositions, which yields negligible melt fractions (<~10%) for similar temperatures. A particular focus of this study is residual monazite, which preferentially incorporates light rare earth elements (LREE) and Th, thereby exerting a powerful control on the Th/La ratio of sediment-derived fluids and melts. In contrast to previous studies, we find that $D_{Th/La}$ varies widely and can be significantly above or below unity. Our dataset suggests that this pattern arises because the various members of the monazite solid solution series are influenced independently by different parameters. We also demonstrate that monazite–melt partition coefficients based on doped experiments cannot be used uncritically to predict fractionation processes in nature because of monazite–huttonite solid solution. However, extrapolation of our results to natural concentration levels suggests fractionation of Th from La in the presence of monazite in most cases. We propose that a solid residue with little or no residual monazite is needed to explain a wide range of geochemical features of arc magmas, including Th/La ratios. A monazite-free residue can be achieved at relatively low sub-arc temperatures provided that enough water is made available (e.g. through antigorite breakdown) to promote sufficient melting to dissolve the entire LREE + Th budget of the sediment.

KEY WORDS: *subduction; sediment; monazite; Th/La; U/Th disequilibria*

INTRODUCTION

Subduction progressively heats and compresses relatively low-temperature lithospheric materials through a succession of metamorphic reactions, releasing H_2O-rich fluids or melts, and certain trace chemical components, to the overlying plate. Conceptually, the process of subduction zone magmatism is widely accepted; however, some key details remain poorly known. For example, there is a continuing debate in the literature about the nature of the liberated fluids that are ultimately responsible for arc magmatism (siliceous fluids, hydrous melts, supercritical fluids), and on their origin [serpentinized lithospheric mantle, hydrated mid-ocean ridge basalt (MORB), oceanic sediment] (e.g. Pawley & Holloway, 1993; Ulmer & Trommsdorff, 1995; Schmidt, 1996; Elliott *et al.*, 1997; Tatsumi & Kogiso, 1997; Class *et al.*, 2000;

*Corresponding author. Telephone: +44 117 3315001. Fax: +44 117 9253385. E-mail: Susanne.Skora@bristol.ac.uk

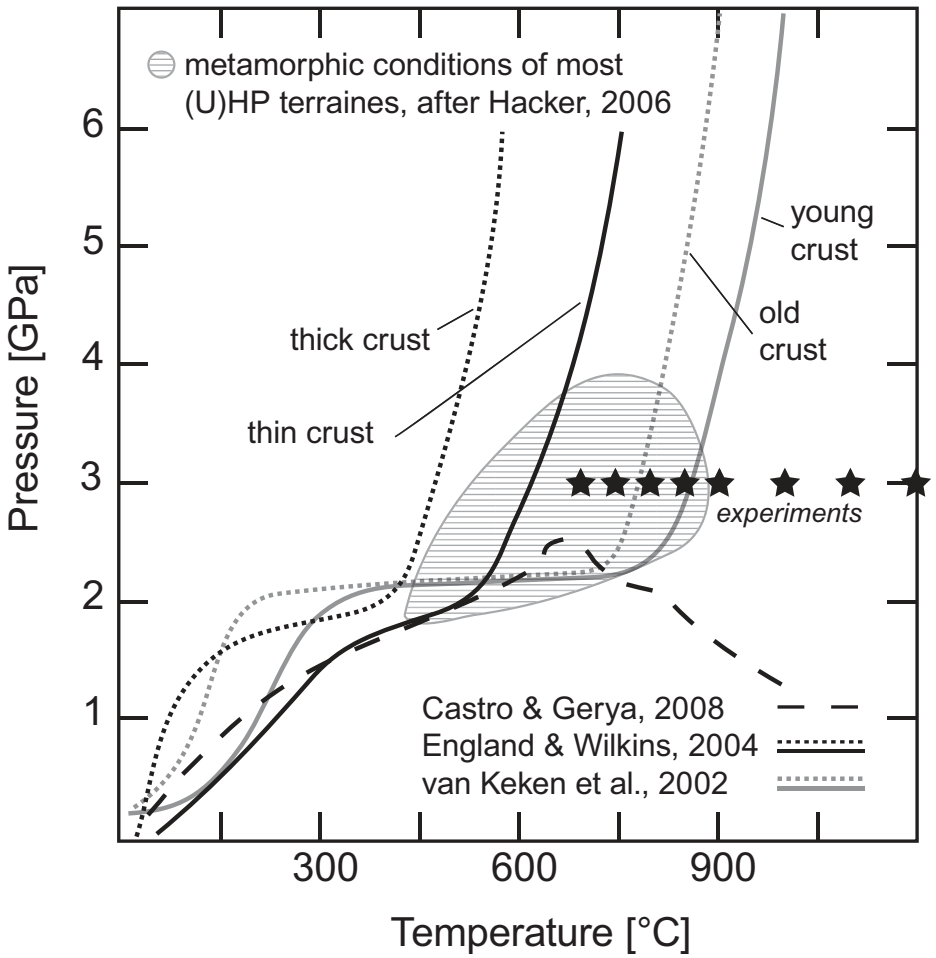

Fig. 1. *P–T* diagram showing geotherms predicted for the top of a subducting slab, using different numerical models (Van Keken *et al.*, 2002; England & Wilkins, 2004; Castro & Gerya, 2008). Variations are due to differences in model assumptions (e.g. mantle properties) and input parameters (e.g. slab ages, velocities, dip angles, frictional heating). It should be noted that variation at any one pressure amounts to several hundred °C. Not all models are able to predict *P–T* conditions recorded in ultrahigh-pressure terrains [shaded area, modified after Hacker (2006)]. Experimental conditions of this study are shown as stars.

Grove *et al.*, 2002; Poli & Schmidt, 2002; Elliott, 2003; Spandler *et al.*, 2003, 2008; Manning, 2004; Kessel *et al.*, 2005*a*; Hermann *et al.*, 2006; Bebout, 2007; Portnyagin *et al.*, 2007; Singer *et al.*, 2007; Bouvier *et al.*, 2008). There is similar uncertainty over the subduction zone geotherm. Depth to the slab in any given arc is generally known to within ± 5 km because of the location of intermediate earthquakes (~80–120 km; England *et al.*, 2004). Prevailing temperatures, however, are much less precisely known, and results of thermal models predict temperatures of between 450 and 900°C at pressures of 2·7–4 GPa, depending on the nature of the model parameters used (Fig. 1). Uncertainty over subduction zone geotherms represents a substantial impediment to physical and chemical modelling.

The diagnostic chemical signature of subduction zone magmas, with their marked depletions and enrichments in certain trace elements, is often attributed to the presence or absence of particular residual phases in the slab. The presence of rutile in subducted crustal rocks prevents the majority of high field strength elements (HSFE, e.g. Brenan *et al.*, 1994; Foley *et al.*, 2000; Zack *et al.*, 2002; Klemme *et al.*, 2005) being released and transferred into the overlying mantle wedge, especially at low slab-top temperatures. This is mirrored in arc volcanic rocks by negative HFSE anomalies (e.g. Pearce & Cann, 1973; McCulloch & Gamble, 1991; Hawkesworth *et al.*, 1993; Thirlwall *et al.*, 1994). Garnets are the major host for the heavy rare earth elements (HREE; e.g. Stalder *et al.*, 1998; Van Westrenen *et al.*, 1999; Green *et al.*, 2000; Pertermann *et al.*, 2004). The behaviour of other important trace elements, such as the light rare earth elements (LREE), uranium (U) and thorium (Th) is less clear. From limited experimental studies and field investigations of subduction

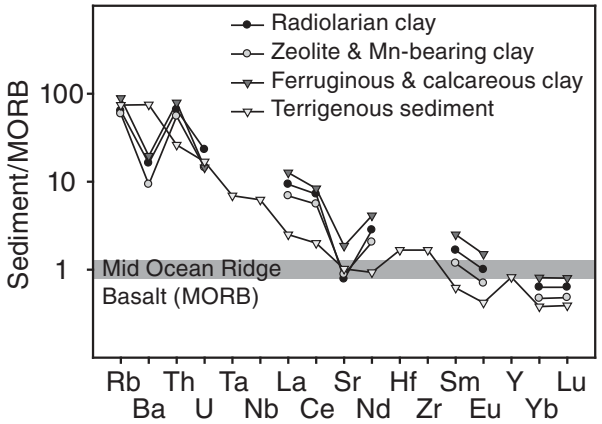

Fig. 2. MORB-normalized trace element diagram for various ocean sediment lithologies [taken from Plank & Langmuir (1998)] subducting below the Lesser Antilles arc. Although there is some inter-sediment chemical variability, key elements such as Th and the LREE are highly enriched in sediments compared with MORB.

zone metamorphic rocks, it is apparent that the large stability field and low solubility of allanite limits the LREE and Th concentration of liberated fluids or melts from the basaltic portion of the slab (e.g. Hermann, 2002; Klimm *et al.*, 2008). This in turn implies that fluids or melts expelled from basalts are unlikely to control the Th and LREE budget of arc volcanic rocks.

Subducted sediments are a particularly potent contributor to the arc geochemical signature because of their initially high trace element abundances relative to subducted mafic crust or the mantle wedge. For example, sediments subducting below the Lesser Antilles arc (Fig. 2), show a strong enrichment in Th, U, La and Ce relative to Atlantic MORB. Plank & Langmuir (1993) demonstrated a clear correlation between the trace element chemistries of subducting sediments and their associated arc volcanic rocks. Although the importance of sediment melting in subduction zones is geochemically widely recognized (e.g. Tera *et al.*, 1986; Plank & Langmuir, 1993; Elliott *et al.*, 1997; Plank, 2005), and some experimental studies exist (e.g. Nichols *et al.*, 1994, 1996; Aizawa *et al.*, 1999; Johnson & Plank, 1999; Schmidt *et al.*, 2004*b*; Auzanneau *et al.*, 2006; Hermann & Spandler, 2008; Thomsen & Schmidt, 2008*a*, 2008*b*; Hermann & Rubatto, 2009), systematic studies on phase relations in the chemically diverse suite of subducting sediments are scant. There are even fewer experimental data on accessory phase stabilities and solubilities in such rocks, and the role that they may play in controlling trace element fluxes. To address this issue, we have conducted high-pressure and -temperature melting experiments on radiolarian clay, an important subducting sediment lithology of the Lesser Antilles and many other arcs (Plank & Langmuir, 1998).

EXPERIMENTAL METHODS

Our experimental procedure largely follows that of Klimm *et al.* (2008). The starting material was a mechanical mixture of pre-dried or fired synthetic oxides, natural albite and carbonates. The main difference is that that we made an initially Al-free starting mix, aiming for a mix that contains structurally bound H_2O. Similar to Klimm *et al.* (2008), we have first mixed reagents in appropriate proportions, which were subsequently decarbonated at 500–1000°C for 6 h. Trace elements were then pipetted in as inductively coupled plasma (ICP) (nitric acid) standard solutions at concentrations above those in natural radiolarian clay (see Table 1 for concentration levels), and subsequently dried under a heat lamp. The resulting mixture was again homogenized in an agate mortar and denitrified at 450°C for 1 h. The decarbonated, denitrified, trace element-doped mixture was pressed into pellets, and equilibrated at 1000°C in a CO–CO_2 gas mixing furnace at an oxygen fugacity of the nickel–nickel oxide (NNO) buffer. We have monitored equilibration by comparing the weight loss owing to conversion of Fe_2O_3 into FeO with a calculated weight loss, assuming a final Fe^{2+}/Fe^{tot} of 0·87 at NNO, 1000°C, 0·1 MPa (calculated using Kress & Carmichael, 1991). After reduction, pellets were homogenized once more before being split into two parts. To one, we have added $Al_2O_3 + Al(OH)_3$ to produce a mix with ~7 wt % H_2O; to the other, we have added Al_2O_3 only. The bulk chemistry of the starting material was checked by analysing a supra-liquidus experiment (~1250°C), with H_2O analysed by secondary ion mass spectrometry (SIMS).

Two systematic sets of experiments were performed: one containing 7 wt % H_2O, with temperature (T) varied from 700 from 1250°C; the other with ~15 wt % H_2O (distilled water added via a microsyringe to the dry mix) and T from 700 to 1000°C. In addition, we performed various experiments with different H_2O contents (Table 2). Our double-capsule technique differed slightly from that of Klimm *et al.* (2008); we loaded identical mixes, including any added H_2O, into both the inner and outer Au ($T = 700$–900°C) or $Au_{80}Pd_{20}$ ($T = 1000$–1250°C) capsules (which were pre-cleaned in acid), to minimize hydrogen diffusion and associated redox. By not using a nickel buffer in the outer capsule, we were able to avoid the Ni–Au–Pd alloying problems that restricted Klimm *et al.* (2008) to $T \leq 900$°C.

All experiments were conducted in half-inch, end-loaded piston cylinder apparatus at Bristol, using the same pressure cell as Klimm *et al.* (2008) (outer sleeves: salt–Pyrex, inner spacer: crushable alumina, friction correction ~3%, McDade *et al.*, 2002). The pressure (P) was set to 3 GPa to match the typical 100 km depth to the Wadati–Benioff Zone beneath arc volcanoes. Similar to Klimm *et al.* (2008), runs were performed using the 'hot piston-in'

Table 1: Composition of experimental starting material, compared with radiolarian clay (from Plank & Langmuir, 1998)

	Rad. clay	RC2	1σ ($n=56$)
SiO_2	61·00	61·49	0·30
TiO_2	0·85	0·87	0·03
Al_2O_3	19·69	19·00	0·18
FeO	8·75	8·90	0·21
MnO	0·19	0·23	0·05
MgO	3·91	3·91	0·07
CaO	1·67	1·76	0·03
Na_2O	2·09	2·02	0·09
K_2O	1·75	1·70	0·04
P_2O_5	0·10	0·11	0·02
			1σ($n=2$)
H_2O	10·5	7·0*	0·5
			1σ($n=5$)
Li		104	2
Sc	*~14*	94	1
V	*~150*	191	1
Sr	88	72	<1
Y	*~24*	36	<1
Zr	*~140*	136	1
Nb	*~18*	143	2
Ba	225	158	2
La	36·34	155	2
Ce	86·59	156	2
Nd	31·55	168	3
Sm	6·22	157	2
Eu	1·34	152	2
Yb	2·47	125	3
Lu	0·37	127	2
Hf	*~4*	45	2
Ta	*~1*	43	2
Th	12·25	216	3
U	1·643	142	3

Major elements were measured using EMPA (wt %), trace elements were measured using SIMS (ppm), given on an anhydrous basis for comparison; 1σ given in wt % or ppm, respectively. Values in italic are estimates from other subducting sediments.
*Analysed by SIMS, $n=2$.

routine; pressure was kept constant manually during runs at ± 0·1 GPa; temperatures were measured with calibrated W_{95}/Re_5–W_{75}/Re_{25} thermocouples, with no allowance for the effect of pressure on e.m.f.; run times were varied with temperature (see Table 2 for full details).

ANALYTICAL TECHNIQUES

Electron microprobe analysis was performed at the University of Bristol, using a Cameca SX-100 (five spectrometers). We have used 15 kV and 15 nA for mineral analysis. Counting times for peaks were usually 30 s and 15 s for background on each side of the peak for silicates, and 20 s and 10 s for melt, respectively. Volatile elements were always measured first. For glass analysis the beam current was reduced to 4 nA; Na was measured for 5 s only, and measurements were performed with a defocused beam (10 μm). Monazite and rutile were measured with a focused spot at 15 kV and 20 nA, and 15 kV and 15 nA, respectively. The combination of low accelerating voltage and beam current sufficiently reduces the excitation volume for the very small experimental grain sizes. Counting times for trace Nb and Ta were increased to 120 s (60 s background), resulting in a detection limit of around 500 and 2200 ppm, respectively. LREE and Th in monazite are present in major amounts; hence counting for 30 s at 15 kV and 20 nA was found sufficient (minimum detection limits: LREE ~1200–3000 ppm; Th ~2800 ppm; U ~2600 ppm; F ~440 ppm). Third-order interferences of phosphorus on F in monazite were resolved by applying an energy window.

SIMS analyses were carried out at the University of Edinburgh, using the NERC Cameca IMS-4f ion-microprobe. Negative oxygen ions were used as the primary ion beam [nominal accelerating voltage 10·5 kV; beam current 4·5 nA; spot size ~15–20 μm; internal standard ^{30}Si; see Klimm *et al.* (2008) for measured isotopes]. An energy filter of 75 ± 20 eV was applied to reduce the transmission of molecular ions. Counting times were adjusted based on expected concentrations such that preferentially over 1000 counts were detected over the course of a single analysis. Subsurface inclusions and contamination were monitored in a count-rate vs time diagram and excluded from the averaging procedure. Oxide interferences were greatly minimized in our experiments by the careful choice of elements and their doping levels. Remaining molecular interferences (e.g. $^{29}Si^{16}O$ on ^{45}Sc) were removed by conventional peak stripping. Ion yields were calibrated on NIST SRM 610 [using concentrations given by Hinton (1990)]; garnet DD1 was analysed as a secondary standard.

We additionally measured trace elements by laser ablation inductively coupled plasma mass spectrometry (LA-ICP-MS) in a few samples with large glass pools, using the facilities of the Bristol Isotope Group (BIG). We employed a New-Wave EXCIMER laser (193 nm) coupled to a Thermo Element 2 with the following settings: frequency 4 Hz; spot size ~20–30 μm; fluency ~2 J cm^{-2}; acquisition times ~30 s (gas blank) and ~60 s (data); standards NIST SRM 610 (external), Ca (internal), BCR-2 and NIST SRM 612 (secondary). Data were

Table 2: Experimental results and calculated proportions of phases (modal %), P = *3 GPa*

Run	h	H_2O	°C	grt	ky	qtz	cpx	phen	ru	ilm	liq	(H_2O)melt	Others
c11	164	7	700	8·6	–	31	23	17	0·4	0·9	–	–	sta, mon
				8·0	–	*29*	*21*	*16*	*0·4*	*0·8*	*5·8*	–	
c16	235	7	750	0·3	20	29	25	17	0·3	4·8	–	–	tlc
				0·3	*19*	*27*	*24*	*16*	*0·3*	*4·5*	*6·0*	–	
c10	123	7	800	23	12	18	12	8·5	0·3	1·7	25	7·6	mon
				21	*11*	*17*	*11*	*8·0*	*0·3*	*1·6*	*30*	*22*	
c23	119	7	850	30	8·5	12	1·2	1·5	0·3	1·4	44	11	mon
				30	*8·3*	*12*	*1·2*	*1·5*	*0·3*	*1·4*	*46*	*15*	
c9	47	7	900	28	10	9·5	–	–	0·2	3·0	49	7·1	mon
				26	*9·7*	*8·9*	–	–	*0·2*	*2·8*	*53*	*13*	
c7	41	7	1000	31	8·7	2·6	–	–	0·2	–	58	9·6	
				30	*8·3*	*2·5*	–	–	*0·2*	–	*59*	*12*	
c8	25	7	1100	23	6·6	–	–	–	–	–	70	8·3	
				22	*6·4*	–	–	–	–	–	*71*	*9·8*	
c12	6	7	1200	19	6·6	–	–	–	–	–	74	8·9	
				19	*6·5*	–	–	–	–	–	*75*	*9·4*	
c15	3	7	1250	–	–	–	–	–	–	–	100	7·0	
				–	–	–	–	–	–	–	*100*	*7·0*	
c17	171	9	800	23	5·2	10	–	18	0·1	3·4	40	12	(mon)
				22	*4·9*	*9·8*	–	*17*	*0·1*	*3·2*	*43*	*19*	
c14	29	13	1000	29	5·3	–	–	–	0·2	–	65	11	
				24	*4·4*	–	–	–	*0·1*	–	*72*	*19*	
c18	167	15	700	6·1	–	29	27	19	0·1	2·6	–	–	sta
				5·2	–	*25*	*23*	*16*	*0·1*	*2·3*	*14*	–	
c22	161	15	750	20	–	23	–	11	0·4	0·5	23	14	sta, am
				18	–	*21*	–	*9·9*	*0·4*	*0·4*	*32*	*47*	
c13	122	15	800	30	10	10	–	5·0	0·7	–	45	14	mon
				25	*8·3*	*8·3*	–	*4·1*	*0·6*	–	*54*	*28*	
c21	73	15	900	36	6·5	2·9	–	–	0·1	–	55	12	(mon)
				29	*5·3*	*2·4*	–	–	*0·0*	–	*63*	*24*	
c20	47	15	1000	31	6·7	–	–	–	0·2	–	60	12	
				26	*5·6*	–	–	–	*0·2*	–	*68*	*22*	

Values in italic are corrected for unmixed fluids (see text for discussion). grt, garnet; ky, kyanite; qtz, quartz; cpx, clinopyroxene (omphacite); phen, phengite; ru, rutile; ilm, ilmenite; gl, glass (see text for definition); sta, staurolite; mon, monazite; tlc, talc; am, amphibole (cummingtonite–anthophyllite). Phase proportions of c13 and c22 are visual estimates. *H_2O is given in wt %.

reduced using GLITTER software. Subsurface inclusions were monitored in a count-rate vs time diagram and excluded from the averaging procedure.

Both datasets, from SIMS and LA-ICP-MS analysis, are in relatively good agreement (usually better than 15%, in agreement with reported values for secondary SIMS standards; see Blundy *et al.*, 1998; Green *et al.*, 2000). The exceptions were U and Th, where SIMS gave systematically low values. We believe that this systematic offset is due to the relatively low formation of Th and U oxide ions in NIST glasses compared with glasses and minerals with lower Si and alkalis (for further discussion, see also, e.g. Blundy *et al.*, 1998; Green *et al.*, 2000). The lower oxide formation is significant because as the oxide formation increases the M^+ peak becomes correspondingly smaller. We have calculated correction factors for both elements based on numerous analyses of various secondary standards (including hydrous granitic glasses), measured at Edinburgh over the last ~15 years (see Supplementary Data File 1, available for downloading at

http://www.petrology.oxfordjournals.org/, for secondary standard data for Th and U, as well as La, Sm, Nb, and Ba, to illustrate typical accuracy and precision). Correction factors of 0·67 for Th and 0·69 for U were applied to all SIMS analyses, and these values bring our SIMS data into agreement (within ~10% for Th and ~15% for U) with ICP-MS analyses of the same samples and anticipated doping levels in our supra-solidus run. It should be noted that the extents of underestimation appear to be consistent from phase to phase for most elements (see Blundy *et al.*, 1998; Green *et al.*, 2000). Therefore, they largely cancel out wherever partition coefficients were calculated using SIMS data only (garnet–melt; melt–bulk solid; melt–whole-rock). This effect should be borne in mind for partition coefficients that are calculated using a combination of EMPA and SIMS data (monazite–melt; rutile–melt).

RESULTS

Phase proportions

Phase proportions in all experimental runs, obtained either by least-square mass balances or by visual estimates, are given in Fig. 3 and Table 2. Representative scanning electron microscope (SEM) images are given in Fig. 4, which also show that melt segregation, probably caused by small temperature gradients in the capsule, occurred in some runs. In addition, Na does not mass balance for the run conducted at 1000°C, containing 15 wt % H_2O, which we believe might have partitioned into the vapour phase upon quenching.

A glass phase is abundant in all experiments at $T \geq 800$°C. Silicate grain sizes increase with temperature and in the presence of a melt phase from micron-sized at 700°C (except for quartz or coesite and garnet) to well-crystallized, 10–80 μm sized grains at higher temperatures. At $T \leq 750$°C, probably metastable phases (such as staurolite and talc) are abundant. Their presence, however, does not alter any of our conclusions, as we focus mainly on trace element evolution of partial melts at $T \geq 800$°C. Major element composition are given in Supplementary Data File 2.

Silicate phases

Garnet occurs in all sub-liquidus runs but its abundances are variable, especially at low temperatures. Two experiments, c18 and c16, appear to contain too little garnet when compared with c11 and c22, performed under similar conditions (Table 2). This is not an uncommon feature in experiments, given that garnet crystallization is known to be affected by sluggish nucleation kinetics. All runs performed at $T \geq 800$°C contained abundant subhedral to euhedral garnet (20–60 μm), which may contain inclusions of other silicate phases. Owing to slow intracrystalline diffusion (e.g. Chakraborty & Ganguly, 1991; Carlson, 2006) compared with growth rates, prograde zoning in experimental garnets is very common and complete equilibration would require unrealistically long run durations. Garnets are enriched in Fe, Mn and Ca in the core region, whereas Mg is enriched at the rims. Consequently, all our interpretations and mass balances are based on garnet rim compositions, as they are closest to being in equilibrium with the matrix, as well as being volumetrically most abundant. End-member calculations reveal that sub-solidus garnets (<750°C; discussed below) are very almandine rich (~59%), with significant pyrope (~24%) and spessartine (4%). The Mg-number [molar Mg/(Mg + Fe)] for those garnets is ~0·3. Super-solidus ($T \geq 800$°C) garnets tend towards essentially binary pyrope–almandine compositions (>90%), with Mg-number ~0·5 and <1% spessartine (Fig. 5). Andradite contents are low in all garnets (<~6 %; Fe^{3+} after Droop, 1987). The very few garnets present in experiment c16 are extremely spessartine-rich (~50–70%). All garnets contain trace Ti, as well as P_2O_5 and Na_2O. Titanium concentrations in garnet in our experiments increase with temperature where Ti is buffered by rutile, a trend that has been noted previously (e.g. Hermann & Spandler, 2008) (Fig. 5). Trace P and Na are probably introduced via the exchange $Na_{+1}P_{+1}$–$X^{2+}_{-1}Si_{-1}$, widely considered to be an ultrahigh-pressure (UHP) indicator (Bishop *et al.*, 1978; Haggerty *et al.*, 1994).

Kyanite occurs in all experiments where metastable staurolite is absent (discussed below). Sizes usually vary within a single experiment from micron-sized to ~80 μm acicular grains. It is rich in iron, with up to ~4·5 wt % Fe_2O_3 and up to ~0·5 wt % MgO. Kyanites contain trace amounts of TiO_2, which, in the presence of rutile, systematically increases from ~0·26 wt % at 800°C to ~0·62 wt % at 1000°C (Fig. 5).

A SiO_2 phase is present in all experiments below $T \leq 1000$°C, 7 wt % H_2O and $T < 900$°C, 15 wt % H_2O. There is a phase transition of quartz–coesite at around 800–850°C, 3 GPa (e.g. Bose & Ganguly, 1995), which is reflected in a morphological change in the SiO_2 phase in our experiments, coesite being tabular in contrast to more rounded quartz crystals (Fig. 4).

Micas are found in all experiments below $T \leq 850$°C, consisting of 2–10 μm sized, mostly euhedral phengite grains. Phengites are muscovite–Al-celadonite solid solutions with negligible $X_{\text{celadonite}}$ (<0·05; Fe^{3+} calculated via charge balance) and $X_{\text{paragonite}}$ (~0·1) components. The (Al)celadonite component [$K(Al,Fe^{3+})(Mg,Fe)Si_4O_{10}(OH)_2$], which increases the phengite Si content at high pressures (e.g. Keller *et al.*, 2005), varies with temperature from ~0·48 at 700°C to ~0·34 at 850°C (Fig. 6). Titanium systematically increases with increasing temperature from ~0·02 wt % at 700°C to 0·05 wt % at 850°C (Fig. 6). Both trends are consistent with experiments in chemically comparable systems

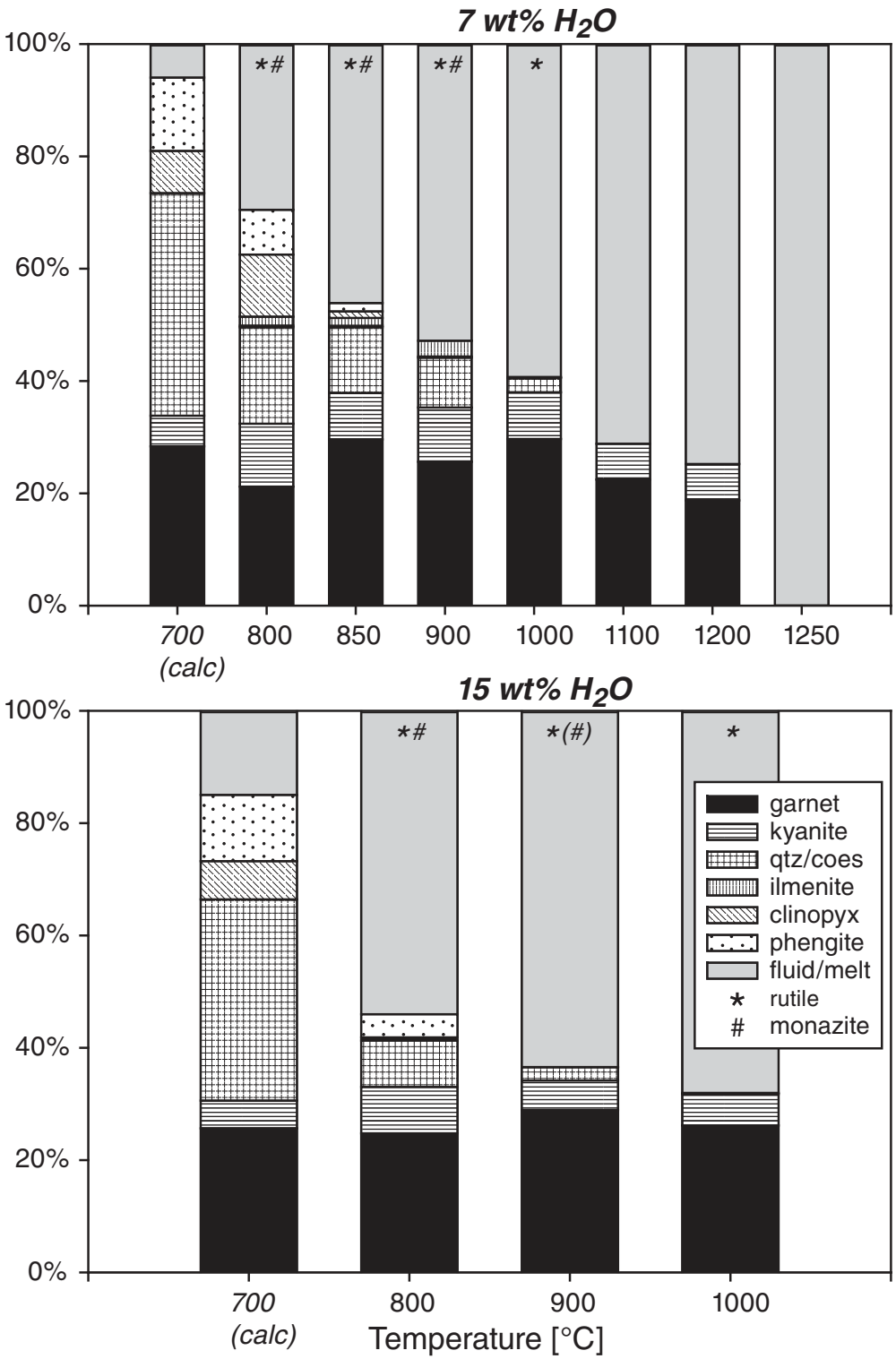

Fig. 3. Phase proportions (in wt %) in our experiments on radiolarian clay at 3 GPa, 7–15 wt % H_2O, as given in Table 2 (plotted are fluid-corrected phase proportions). Sub-solidus assemblages are calculated thermodynamically (see text for details) because these experimental runs contained abundant metastable phases. It should be noted that mass balance, within error, does not give a clear answer as to the presence of monazite in one experiment at 900°C, 15 wt % H_2O.

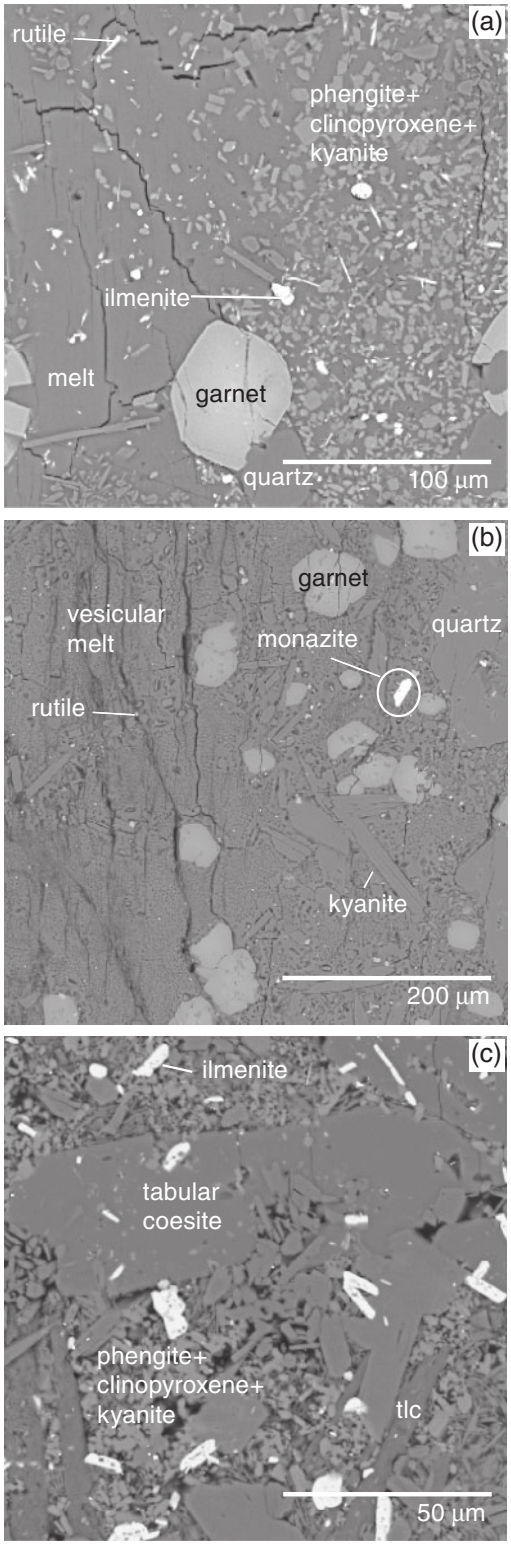

Fig. 4. Backscattered SEM images of representative experimental run products. (a) Garnet + kyanite + quartz + phengite + clinopyroxene + rutile/ilmenite in a hydrous glass matrix formed at 800°C, $H_2O = 7$ wt %. (b) Visibly vesicular glass in low-temperature experiment with high amounts of water present (e.g. 800°C, $H_2O = 15$ wt %). Glass fractions are increased compared with runs at similar conditions but lower bulk water contents [compare (b) and (a)]. (c) Tabular coesite in a sub-solidus run (750°C; $H_2O = 7$ wt %). The morphology changes towards roundish quartz [see (a)] at higher temperatures.

(e.g. Hermann & Spandler, 2008; Auzanneau *et al.*, 2010). Auzanneau *et al.* (2010) have calibrated a Ti-in-phengite thermobarometer for quartz- and rutile-buffered systems, and have identified a coupled substitution involving $Si_{+1}X^{2+}{}_{+1}$–$Al^{IV}{}_{-1}Al^{VI}{}_{-1}$ and $Ti_{+1}Al^{IV}{}_{+1}$–$Al^{VI}{}_{-1}Si_{-1}$ (X^{2+} divalent cation) as exchange mechanisms. No systematic trends with temperature were observed in the paragonite and celadonite components in our limited dataset.

Clinopyroxene occurs as small (≤5 μm) euhedral grains in experiments below 850°C, 7 wt % H_2O and below 750°C, 15 wt % H_2O. Because of the small grain size, it is difficult to evaluate whether compositional zoning is present, such as that observed in experiments by Hermann & Spandler (2008), in which clinopyroxenes appear to have higher Fe contents in the core. All clinopyroxenes are omphacites with $X_{jadeite} \sim 0{\cdot}5$ and a small aegirine component [<5%; Fe^{3+} after Droop (1987); definition and site assignment after Morimoto *et al.* (1988)]. The small excess Na over Al correlates with Fe^{3+}, confirming that solely jadeite and acmite exchange vectors were operative. Again, no systematic compositional trends with temperature were visible in our limited dataset.

Metastable phases and subsolidus phase equilibria

We conducted two experiments at $T = 700$ and 750°C with 7 and 15 wt % H_2O, respectively. In comparison with experiments at higher T, these experiments appear to be unsystematic and yielded ambiguity as to the sub-solidus phase assemblage. These experiments were composed of abundant coesite and phengite. Fe-rich staurolite is abundant (~14–18%) in three out of four low-T experiments, as tabular grains up to 30 μm across. Where staurolite is present, kyanite is absent. Two staurolite-bearing experiments ($T = 700$°C, 7 wt % H_2O; $T = 700$°C, 15 wt % H_2O) are characterized by low garnet contents (<~5%). Although staurolite may occur at UHP conditions in basic rocks (e.g. Hellman & Green, 1979; Klimm *et al.*, 2008), studies on the stability of staurolite in a pelitic system suggest that almandine + kyanite should be stable in preference to Fe-rich staurolite at run conditions (e.g. Richardson, 1968; Ganguly, 1972; Ballevre *et al.*, 1989). Hence, we interpret staurolite to have nucleated metastably. The other experiment with staurolite ($T = 750$°C, 15 wt % H_2O) contains amphibole that is cummingtonite–anthophyllite in composition [Fe^{3+} after Droop (1987); definition and site assignment after Leake *et al.* (1997)], which is also unlikely to be stable at run conditions. Clinopyroxene is absent in

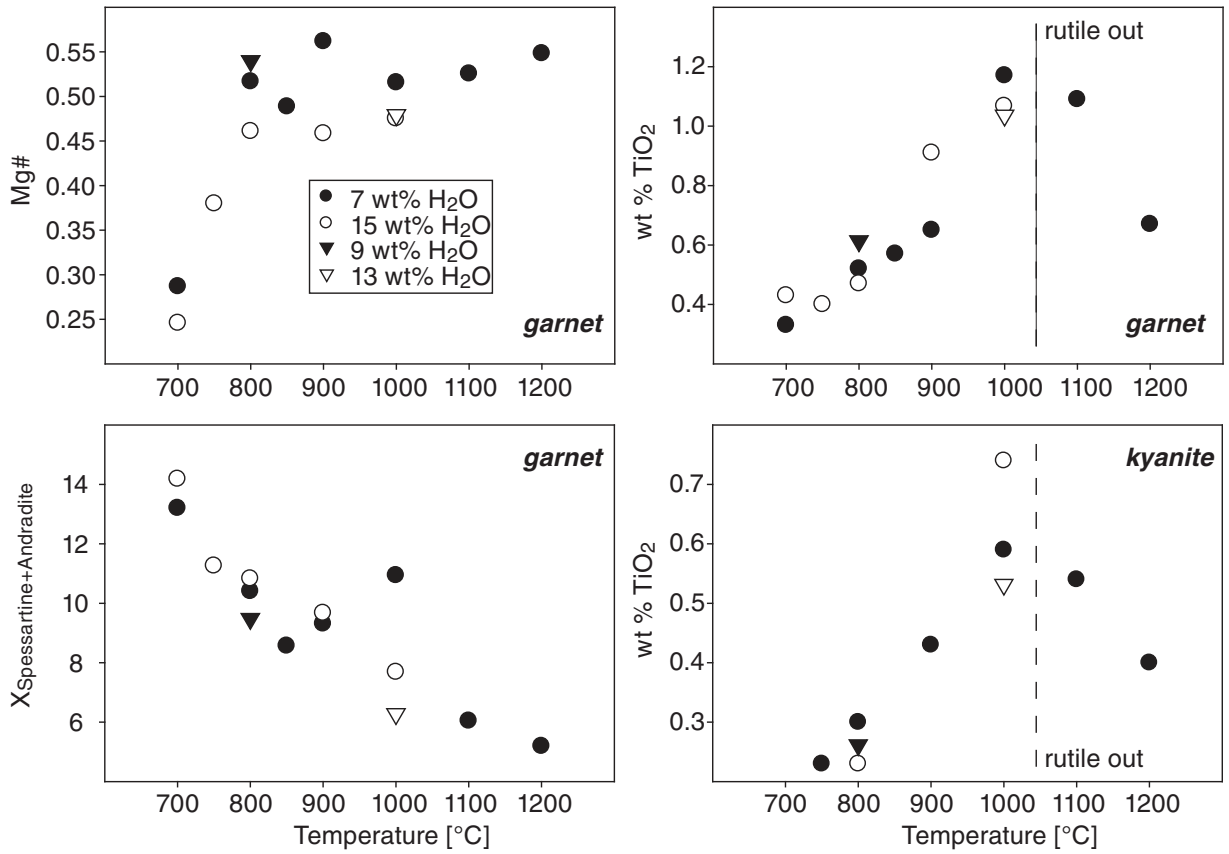

Fig. 5. Left, garnet chemistry as a function of temperature, expressed in terms of Mg-number and $X_{\text{Spessartine +Andradite}}$; right, increasing TiO_2 in garnet and kyanite with increasing temperature in the presence of rutile.

this experiment, which is counterbalanced by very high Na contents in the melt phase and by an enhanced $X_{\text{paragonite}}$ in phengite. The fourth experiment at $T \leq 750^{\circ}C$ ($T = 750^{\circ}C$, 7 wt % H_2O) without staurolite also has a low garnet content, but has crystallized more clinopyroxene and talc instead, which we also interpret to have formed metastably.

It appears that sluggish nucleation, especially for garnet, at sub-solidus conditions is responsible for the crystallization of metastable staurolite, talc and/or cummingtonite–anthophyllite. Circumventing this problem probably requires the use of gel or glass starting mixtures and substantially longer run durations. Instead, we have calculated thermodynamically the equilibrium sub-solidus phase assemblage for our chosen chemistry (excluding trace Mn, Ti and P). Calculations were performed for water-saturated radiolarian clay, using the Theriak software package (De Capitani, 1994). We used two databases: (1) the updated thermodynamic database of Berman (1988); (2) the updated thermodynamic database of Holland & Powell (1998), as distributed with the software (databases: jun92 and tc32lp2, respectively). Despite using different databases with different solid solutions, the calculated sub-solidus phase assemblage and proportions at 700°C and 750°C, 3 GPa, agree remarkably well (±1%): garnet, kyanite, clinopyroxene, phengite, coesite and H_2O, consistent with other experiments (e.g. Schmidt *et al.*, 2004*b*). We have chosen to adopt these calculated sub-solidus assemblages, in preference to the experimental metastable ones, in subsequent discussions.

Glass phase

A glass phase was identified in all experiments at $T \geq 750^{\circ}C$, 15 wt % H_2O and $T \geq 800^{\circ}C$, 7 wt % H_2O. It is possible that the metastable presence of another hydrous phase (e.g. talc) inhibited melting to observable degrees in the experiment at $T = 750^{\circ}C$, 7 wt % H_2O. The run conducted at $T = 750^{\circ}C$, 15 wt % where melt was present, however, did contain metastable phases combined with the absence of otherwise widespread clinopyroxene in low-T runs. We propose that the wet solidus of radiolarian clay at 3 GPa is at ~750°C or slightly below, which is just above the solidi given by Nichols *et al.* (1996) and Hermann & Spandler (2008) for the same pressure,

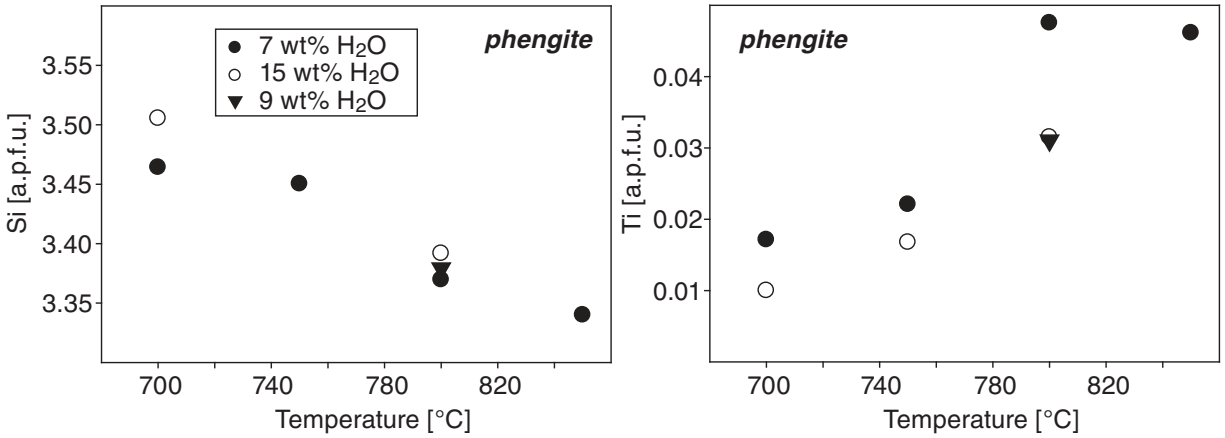

Fig. 6. Si and Ti (a.p.f.u.) in phengite, in equilibrium with rutile, as a function of temperature.

but considerably lower than that of Johnson & Plank (1999). The 3 GPa liquidus lies between 1200 and 1250°C.

An important issue is whether fluids at our run conditions were siliceous H_2O-rich vapours, hydrous silicate melts or supercritical fluids, especially as mass-balance calculations (using H_2O by difference in the glasses) indicate that water does not mass balance. We used double capsules with similar water contents in the inner and outer capsule to minimize H_2O loss or gain through H_2-mediated redox reactions. In addition, run durations were reasonably short, further minimizing H_2 diffusion. We therefore conclude that, similar to the experiments of Klimm *et al.* (2008) with high water contents, either a single supercritical fluid phase unmixes upon quenching or that two fluid phases (hydrous melt + siliceous fluid) coexisted at run conditions—both explanations will result in a separate condensed vapour phase after quenching that will be lost during sample preparation.

The arguments of Klimm *et al.* (2008) in favour of a supercritical fluid were based on optical observations such as the presence of highly vesicular glasses. Our quenched glasses appear only partly vesicular (at $T \leq 800$°C, ≥ 9 wt % H_2O where the ratio melt/vapour phase is smallest) (Fig. 4). Other experimental glasses contain abundant fine cracks that might have provided pathways for an additional vapour phase to escape. Whether two fluid phases or a single fluid phase existed at run conditions depends on whether (1) the melt phase was water-saturated for a given bulk water content or (2) the second critical endpoint was overstepped for our melt composition. Published experimental data (e.g. Bureau & Keppler, 1999; Hermann *et al.*, 2006; Hermann & Spandler, 2008; Klimm *et al.*, 2008) suggest supercritical behaviour for haplogranites at $T \geq 750$°C, 3 GPa. Our data actually suggest sub-critical behaviour, at least for lower temperatures (<~900°C, discussed below). In any case it is likely that a single fluid phase was present at run conditions, given that the maximum water content of melts in this study is <30 wt % H_2O in runs at $T \geq 800$°C (Table 2), and that the miscibility gap at high pressures is located at rather high water contents when approaching the second critical endpoint. [For example, for MORB, the miscibility gap at 4 GPa (second critical endpoint at 6 GPa) starts at > 35 wt % H_2O in the melt (Kessel *et al.*, 2005*b*)]. This suggests that during quenching, the liquid in our capsules separated into a fluid–vapour phase and a hydrous melt or glass and hence must be corrected to its unmixed fluid state. Chemical compositions and phase proportions given in Table 2 are consequently given twice: once as measured and once to include the unmixed fluid phase (compare Klimm *et al.*, 2008). We emphasize that whether the fluid phase is supercritical or not has very little bearing on our conclusions concerning trace element transport. In the ensuing discussion we will refer to the liquid phase as 'melt', when considering its high-T behaviour, or 'glass' when discussing its quenched-phase chemistry. We will further refer to 'fluids' when considering water (± trace dissolved elements), or if the nature of the HP liquid is unknown.

Our experiments confirm that high-pressure melts in equilibrium with calcium-poor metapelites are essentially peraluminous, Mg-poor granites with molar Al > Na + K + Ca (Table 3). In general, aluminium saturation indices (ASI) are ~1·3 in melts generated just above the solidus, and increase with increasing temperature towards the starting material value of ~2·8. Glasses are relatively homogeneous with 1σ for major elements typically <10% relative. In addition, no quench crystal phases were observed, indicating that the glass composition has not been significantly modified upon quenching. The SiO_2 content decreases slightly from 750 to 1000°C and then markedly at higher temperatures (Table 3; Fig. 7). This trend is mirrored by an increase in FeO. The TiO_2 content in the glass increases steadily from 750 to 1100°C, reflecting

Table 3: Major element composition of experimental quenched glasses

Run:	c10		c23		c9		c7		c8		c12	
°C:	800		850		900		1000		1100		1200	
H_2O:	7		7		7		7		7		7	
Melt:	$n=14$	1σ	$n=30$	1σ	$n=21$	1σ	$n=34$	1σ	$n=39$	1σ	$n=32$	1σ
SiO_2	76·17	1·00	75·65	0·91	75·34	0·61	75·23	0·70	71·13	0·39	69·35	0·28
TiO_2	0·23	0·02	0·18	0·06	0·42	0·13	0·51	0·03	1·02	0·02	0·99	0·03
Al_2O_3	13·82	0·58	14·30	0·27	14·21	0·36	13·37	0·46	14·53	0·10	14·87	0·09
FeO	1·35	0·35	1·11	0·13	1·40	0·09	2·52	0·44	4·70	0·09	6·02	0·13
MgO	0·46	0·12	0·59	0·05	0·31	0·02	0·68	0·17	1·41	0·05	1·82	0·05
MnO	0·02	0·02	0·05	0·06	0·01	0·01	0·03	0·02	0·07	0·02	0·14	0·03
CaO	0·84	0·22	0·99	0·05	0·75	0·02	1·28	0·04	1·88	0·02	1·93	0·02
Na_2O	3·88	0·30	4·07	0·25	3·42	0·37	3·12	0·12	2·66	0·17	2·50	0·06
K_2O	3·16	0·30	2·99	0·09	4·06	0·09	3·14	0·08	2·47	0·05	2·26	0·04
P_2O_5	0·08	0·02	0·07	0·04	0·07	0·03	0·11	0·03	0·12	0·02	0·12	0·03
ASI	1·31	0·10	1·32	0·06	1·33	0·08	1·38	0·06	1·66	0·06	1·79	0·03
Run:	c17		c14		c22		c13		c21		c20	
°C:	800		1000		750		800		900		1000	
H_2O:	9		13		15		15		15		15	
Melt:	$n=9$	1σ	$n=46$	1σ	$n=8$	1σ	$n=41$	1σ	$n=25$	1σ	$n=9$	1σ
SiO_2	76·50	1·86	74·14	1·13	76·66	0·99	78·01	1·62	76·92	1·10	77·62	0·23
TiO_2	0·15	0·01	0·59	0·02	0·06	0·03	0·13	0·01	0·22	0·04	0·45	0·01
Al_2O_3	14·49	0·37	14·63	0·98	12·11	0·24	12·82	0·27	13·28	0·19	13·73	0·11
FeO	0·95	0·10	2·73	0·13	0·87	0·50	1·10	0·11	1·22	0·14	2·33	0·05
MgO	0·55	0·08	1·21	0·04	0·41	0·45	0·73	0·06	0·57	0·03	0·69	0·02
MnO	0·01	0·01	0·07	0·03	0·03	0·04	0·04	0·03	0·05	0·05	0·04	0·02
CaO	0·92	0·05	1·75	0·05	1·37	0·22	0·61	0·07	0·97	0·05	1·31	0·01
Na_2O	4·06	0·59	2·12	0·23	6·43	0·67	3·61	0·22	3·45	0·39	0·93	0·13
K_2O	2·30	0·20	2·64	0·06	1·83	0·15	2·88	0·10	3·25	0·12	2·80	0·04
P_2O_5	0·08	0·02	0·12	0·02	0·24	0·06	0·06	0·02	0·07	0·04	0·09	0·02
ASI	1·45	0·15	1·84	0·15	0·88	0·07	1·33	0·06	1·32	0·09	2·38	0·09

All analyses in wt % oxides, given on an anhydrous basis. Errors = 1σ of multiple (*n*) analysis.

enhanced rutile solubilities at higher temperatures (Table 3; Fig. 7) (e.g. Ryerson & Watson, 1987). Given that rutile is not actually present at 1100°C, the increase from 1000 to 1100°C may imply that rutile is exhausted closer to 1100°C than 1000°C. The K_2O content steadily increases in the presence of phengite, reaching a peak at $T \sim 900$°C, just above the upper stability of phengite in our experiments (Table 3; Fig. 7). Na_2O appears to decrease steadily with increasing temperature despite the presence of omphacite at $T = 800$–850°C, 7 wt % H_2O (Table 3). We note, however, that the experiment conducted at $T = 750$°C, 15 wt % H_2O lacks clinopyroxene and has metastable phases (staurolite + orthoamphibole), which probably caused high excess Na_2O in the melt phase (ASI ~0·9) (Table 3).

Phase proportions and the melting reaction

Phase proportions are given in Fig. 3 and Table 2. We note that corrections for unmixed water are subject to potentially high errors (e.g. water estimates owing to the difference method; uncertainties in mass balance), but corrections may be important, for example, to identify positive or

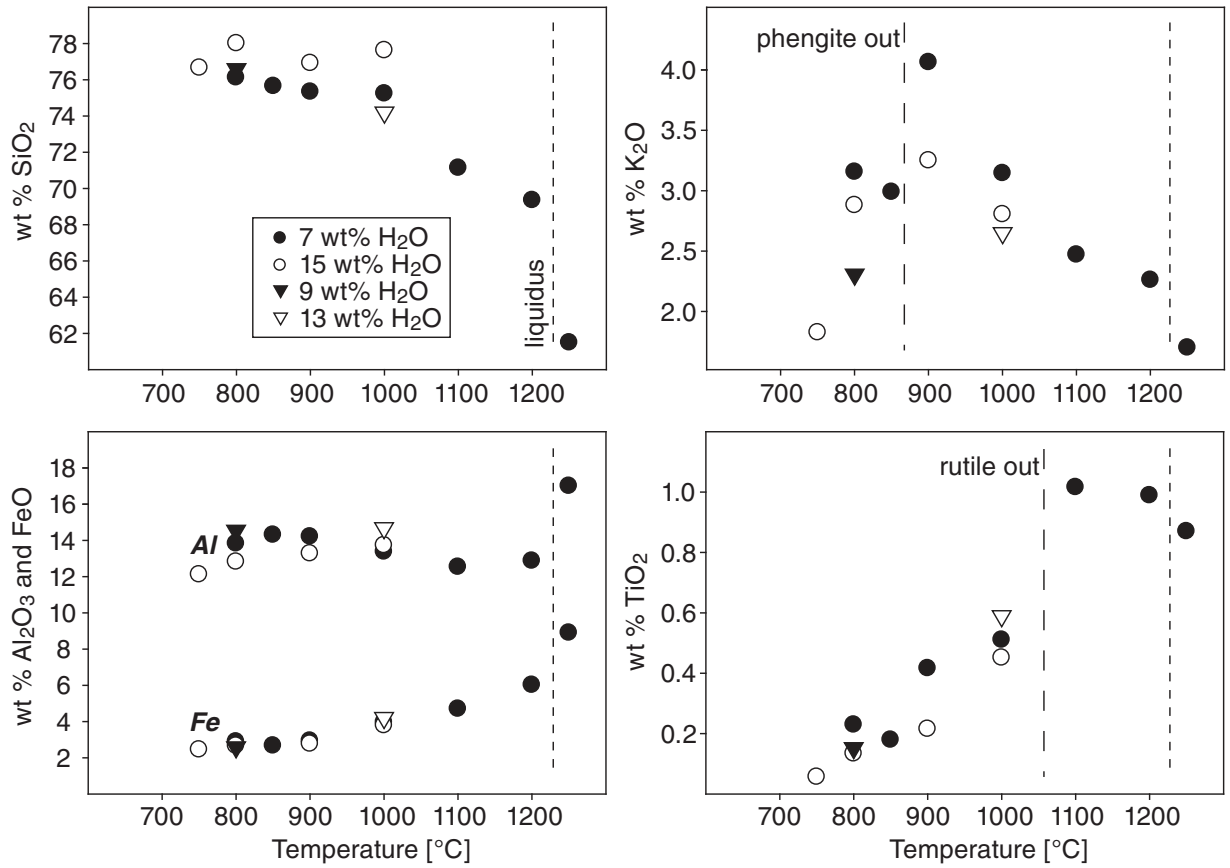

Fig. 7. Major element chemistry of quenched glasses (on anhydrous basis) from this study as a function of temperature. Data from Table 3.

negative changes in phase proportions with changing temperature.

Phase proportions show systematic changes with temperature. The sub-solidus assemblage contains garnet, kyanite, clinopyroxene, phengite, coesite and an excess fluid phase whose amount depends on the initial H_2O content less structurally bound water in phengite (~0·5%). With increasing temperature, the modal amount of SiO_2 + clinopyroxene + phengite decreases steadily, accompanied by a steady increase in the melt phase. The amount of garnet and kyanite varies less systematically, but overall garnet modes increase and peak at $T = 1000°C$ where clinopyroxene + phengite are exhausted and SiO_2 (quartz) occurs only in trace amounts. Significant changes in garnet composition (Mg-number) above the solidus (Fig. 5) occur, implying that garnet chemically takes part in the melting reaction. In combination, our data suggest an initially incongruent melting reaction at $T < \sim 1000°C$ that consumes phengite, clinopyroxene, SiO_2 and H_2O and forms garnet, kyanite and melt (see Schmidt, 1996; Hermann & Green, 2001; Poli & Schmidt, 2002; Hermann & Spandler, 2008). Above 1000°C, there is a change in the melting reaction, with melt fraction increasing at the expense of garnet and kyanite. This coincides with a significant change in the melt composition (e.g. strong increase in FeO; Fig. 7), consistent with Fe-rich garnet being consumed.

Although the general pattern of phase relations in both experimental sequences (7 and 15 wt % H_2O) looks very similar, there is a remarkable difference in the melt fraction that is generated at low temperatures. Figure 8 shows melt fraction vs temperature, assuming that the solidus is at $T = 750°C$. Melt productivity has a steep trend at 7 wt % H_2O until around 850–900°C, above which the trend flattens. Approximately 50% of the melt is generated within the first ~100–150°C above the solidus, whereas further melting from 900 to 1200°C produces only a further 25%. Melt productivity occurs along an even steeper slope in experiments with 15 wt % H_2O, where >50% of melt is generated within the first ~50°C above the solidus. At higher temperatures the melt fraction curve has a flatter slope, with an increase in the melt fraction from ~55 to only 70% over 200°C. It appears that when the melt fractions in the two experimental sequences are compared isothermally, the differences in melt fraction at $T = 900$–1000°C approximately equal the excess H_2O; however,

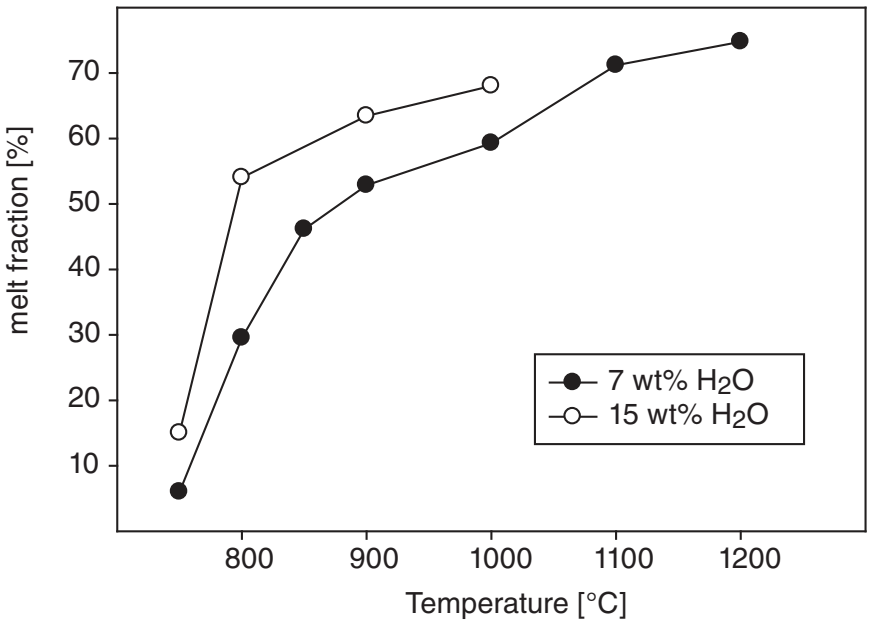

Fig. 8. Fluid-corrected melt fractions (as calculated from mass balance) for both experimental sequences (7 and 15 wt % H_2O) as a function of temperature. Data from Table 2.

the presence of melt at 800°C is clearly enhanced by a factor of two in the sequence with higher H_2O. This melting behaviour is reminiscent of a binary H_2O–silicate system in which there is a eutectic, at least for near-solidus temperatures. The presence of a eutectic is more consistent with sub-critical than supercritical behaviour (e.g. Kessel *et al.*, 2005*b*).

Accessory phases

Compositions of accessory phases are given in Supplementary Data File 3. Rutile is present in all runs at $T \leq 1100$°C. Grains are usually 1–2 μm in size and roundish in shape with trace amounts of SiO_2 (<~1 wt %) and Al_2O_3 (~1 wt %), as well as significant FeO (~6 wt %). The amount of rutile steadily decreases with increasing temperature, reflecting its increased solubility, until it is exhausted above 1000°C. Fe–Ti oxides (ilmenite) were identified in most runs at $T < 1000$°C. They are typically >2 μm in size, tabular to acicular in shape, and contain significant hematite (>50 %) with minor MgO (~0·6 wt %) and Al_2O_3 (~1·2 wt %).

Above the solidus, monazite was identified in all runs at $T \leq 900$°C, 7 wt % H_2O, and $T \leq 800$°C, 15 wt % H_2O; its presence is inferred from mass balance for $T = 900$°C, 15 wt % H_2O and for $T = 800$°C, 9 wt % H_2O. Similar to rutile, monazite is exhausted at $T > 900$°C because of the temperature dependence of monazite solubility in silicate melts (e.g. Rapp & Watson, 1986). Below the solidus, a single grain of monazite was identified in only one run ($T = 700$°C; 7 wt % H_2O). Apatite, an alternative host for LREE + Th and sometimes related to monazite formation (e.g. Wolf & London, 1995), was never observed, despite the presence of phosphorus. Allanite, which is also often reported as a precursor to monazite (e.g. Janots *et al.*, 2007), also was never detected. The absence of apatite and allanite are plausibly related to the low Ca content of the starting material. It is also unlikely that the total LREE + Th could have been dissolved into any of the other stable or metastable silicate phases. We therefore believe that monazite was saturated at sub-solidus conditions at around 700–750°C, 3 GPa. It is likely that positive identification of monazite was hindered by the generally very small grain sizes in sub-solidus runs.

Monazites rarely exceed 2 μm in size. The larger grains clearly exhibit some zoning that varies from irregular and patchy to sector-zoning. Similar zoning patterns have been reported from many naturally occurring monazites (e.g. Zhu & O'Nions, 1999; Townsend *et al.*, 2000; Yang & Pattison, 2006). Monazites are LREE-monazite ($LREEPO_4$)–huttonite ($ThSiO_4$)–brabantite ($Ca_{0·5}Th_{0·5}PO_4$) solid solutions (e.g. Bowie & Horne, 1953; Förster, 1998; Förster & Harlov, 1999; Spear & Pyle, 2002). (There is also a U equivalent to the monazite–huttonite substitution, with U taking the place of Th [coffinite $(USiO_4)_{1-x}(OH)_{4x}$] solid solution (e.g. Williams *et al.*, 2007).) Our experimental monazites are highly variable in composition. They either have an $X_{monazite}$ of ~0·6–0·7 and approximately equal amounts of $X_{huttonite}$ and $X_{brabanite}$, or have lower $X_{monazite}$ of ~0·5 and major $X_{huttonite}$ (~0·4–0·5) (Fig. 9). Compositions can vary

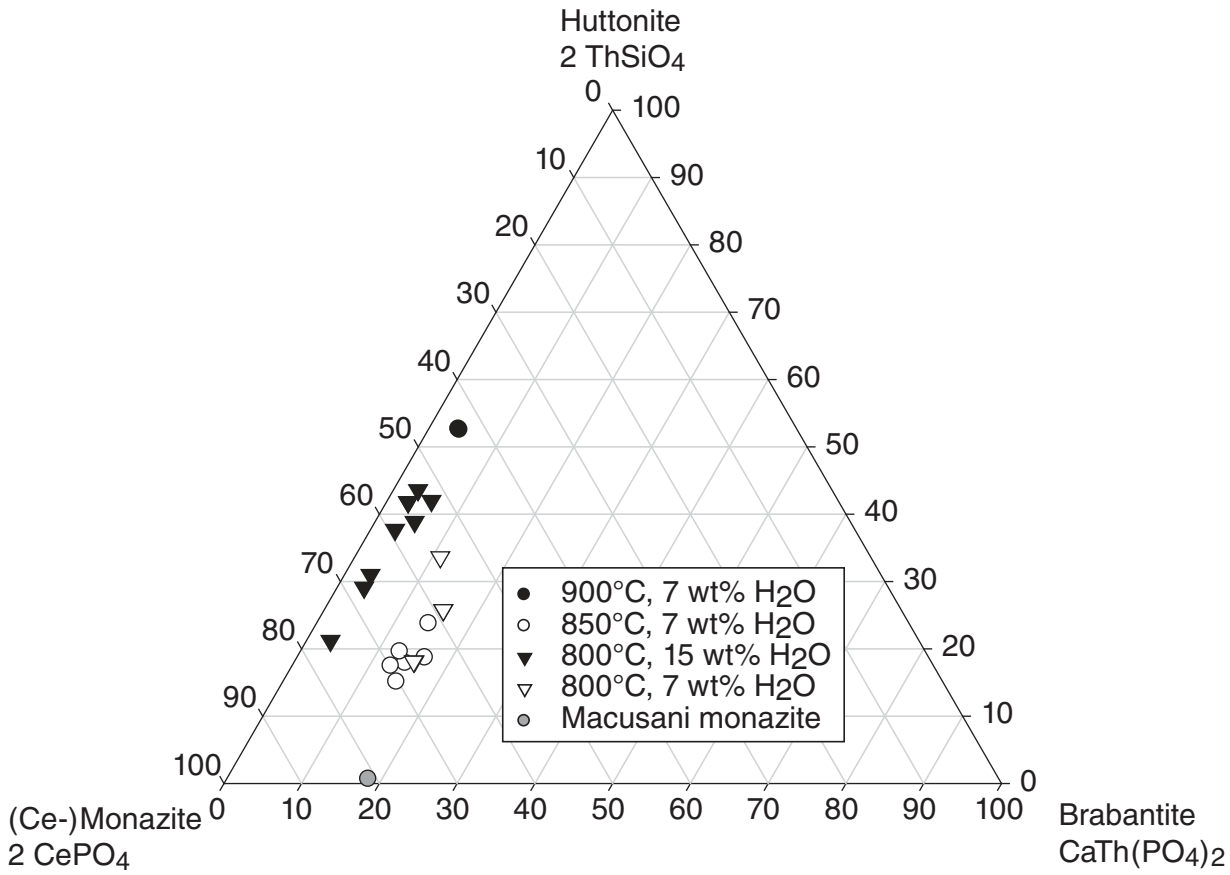

Fig. 9. Monazite compositions in this study, plotted into the Ce-monazite (Ce)–huttonite ($ThSiO_4$)–brabantite ($Ca_{0.5}Th_{0.5}PO_4$) ternary (U was added to Th for the calculations). Also shown is a natural monazite phenocryst from Macusani (Pichavant *et al.*, 1987; Montel, 1993).

appreciably even within a single experiment, consistent with individual larger grains being zoned. We have therefore measured several spots per grain where possible, and present mean analyses in Fig. 9. Monazites contain trace amounts of F (~0·5 wt %), and appreciable U (~0·15 atoms per formula units, a.p.f.u.) substituting for Th.

The presence of trace amounts of zircon is suggested by mass-balance calculations in experiments at $T \leq \sim 850^{\circ}C$, but this was never identified positively by SEM.

Trace element partitioning

Trace element abundances in glass pools (Table 4) and garnets (Supplementary Data File 4) were analysed by SIMS, and REE, Th and U, and Nb and Ta in monazites (Table 5) and rutile (Supplementary Data File 5), respectively, were analysed by electron microprobe. The effect of doping the starting materials with LREE and Th on monazite stability and partitioning is discussed in a section below.

Glasses are relatively homogeneous with respect to trace elements, with 1σ on 4–5 analysis spots typically <10% relative. Glasses are generally enriched in 'fluid-mobile' elements such as Sr and Ba, and depleted in elements that are retained by accessory phases (rutile, monazite) and garnet. As expected, garnets are major hosts for HREE, Y and Sc. Monazite is the major host for LREE (La–Eu; Gd was not added) and Th in all runs at $T \leq 900^{\circ}C$. Rutile is the major host for Ti, Nb and Ta. Phengite is the major host of K, and although not measured, should be the major host for other large ion lithophile elements (LILE; e.g. Ba, Cs, etc.; Domanik & Holloway, 1996; Schmidt, 1996; Sorensen *et al.*, 1997; Melzer & Wunder, 2000; Zack *et al.*, 2001; Hermann, 2002; Schmidt *et al.*, 2004*b*; Hermann & Rubatto, 2009). All mineral–melt partition coefficients are calculated using the fluid-corrected trace element composition of quenched glasses (i.e. taking account of exsolved H_2O on quenching).

Garnet–melt partitioning

Although core-to-rim trace element zoning could not be determined, garnet trace element zoning is to be expected because of slow intracrystalline diffusion rates

Table 4: Trace element composition of experimental quenched glasses

Run:	c10		c23		c9		c7		c8		c12	
°C:	800		850		900		1000		1100		1200	
H_2O:	7		7		7		7		7		7	
Melt:	$n=5$	1σ	$n=4$	1σ	$n=6$	1σ	$n=5$	1σ	$n=5$	1σ	$n=4$	1σ
Li	134	32	187	96	210	36	189	8	162	2	145	1
K*	22500	2120	24200	740	31500	700	25500	610	20200	400	18700	330
Sc	3·1	0·2	5·1	0·2	3·4	0·2	14·9	0·7	19·7	0·4	25·9	0·6
Ti*	825	91	927	315	1360	430	2700	140	5490	120	5370	140
V	61	5	99	12	88	9	121	2	161	1	176	4
Sr	200	6	190	5	166	5	131	5	107	1	98	2
Y	2·3	0·3	2·6	0·2	1·5	0·4	10·7	0·4	14·6	0·3	19	1
Zr	75	6	94	5	106	21	138	5	158	1	158	3
Nb	22	3	84	71	71	6	100	4	199	1	193	4
Ba	276	12	309	11	384	12	299	12	246	2	224	4
La	69	13	91	5	185	11	270	10	227	2	212	6
Ce	66	13	89	6	181	11	268	12	231	3	215	7
Nd	65	11	85	4	142	9	231	10	235	2	224	7
Sm	54	8	59	2	65	6	130	5	190	2	192	5
Eu	47	4	49	1	44	5	106	4	167	1	173	5
Yb	1·8	0·5	3·8	0·6	1·5	0·7	14·7	0·9	21·3	0·9	32	2
Lu	1·3	0·5	3·4	0·8	1·2	0·6	11·6	0·5	16·8	0·5	26	2
Hf	43	5	50	4	57	8	59	3	60	2	58	3
Ta	7	2	26	14	23	3	32	3	64	1	61	2
Th	179	16	261	10	349	42	438	17	347	3	315	9
U	285	21	272	14	268	21	258	12	214	2	195	4
Ba/La_n	3·93	0·76	3·31	0·23	2·03	0·14	1·09	0·06	1·06	0·02	1·04	0·04
Th/La_n	1·83	0·38	2·01	0·15	1·33	0·18	1·14	0·07	1·08	0·03	1·05	0·05
Zr/Hf_n	0·57	0·09	0·62	0·07	0·61	0·15	0·77	0·06	0·86	0·05	0·90	0·06
Nb/Ta_n	0·92	0·26	0·96	0·96	0·91	0·16	0·94	0·10	0·93	0·04	0·94	0·05
Th/U_n	0·38	0·04	0·58	0·04	0·78	0·11	1·02	0·06	0·98	0·03	0·97	0·04

Run:	c15		c17		c14		c13		c21		c20	
°C:	1250		800		1000		800		900		1000	
H_2O:	7		9		13		15		15		15	
Melt:	$n=5$	1σ	$n=3$	1σ	$n=3$	1σ	$n=5$	1σ	$n=6$	1σ	$n=5$	1σ
Li	104	2	140	53	97	47	111	21	33	7	171	1
K*	14100	340	17600	1550	19900	490	19900	700	23300	890	20600	280
Sc	93·6	1·0	4·6	0·6	11·9	0·3	5·5	0·6	7·8	0·1	10·7	0·3
Ti*	4900	152	725	59	2860	87	577	51	981	171	2100	59
V	191	1	81	4	52	1	67	1	23	28	63	1
Sr	71·9	0·6	158	3	98	1	126	3	108	5	109·9	0·4
Y	35·9	0·3	0·7	0·1	5·0	0·1	1·9	0·1	4·5	0·3	4·9	0·1
Zr	136	1	73	4	118	3	51	3	96	8	102	3
Nb	143	2	36	1	131	4	31	2	68	7	94	8
Ba	158	2	249	9	222	4	245	11	249	16	247	3
La	155	2	46	4	206	5	130	7	200	15	217	4
Ce	156	2	45	3	206	5	131	8	195	15	213	5
Nd	168	3	47	3	186	5	116	7	130	11	164	3
Sm	156	2	34	3	110	2	56	3	42	2	76	2
Eu	152	2	22	2	90	2	29	2	42	3	70	1
Yb	125	3	0·5	0·3	10·1	0·8	5·9	0·4	5·6	0·4	7·5	0·4
Lu	127	2	0·6	0·0	8·7	0·5	7·2	0·5	4·7	0·4	8·3	4·7
Hf	45	2	44	3	47·2	0·7	29	2	48	5	45	3
Ta	43	2	14	1	37	2	10·2	0·5	22	2	31	2
Th	219	3	157	12	325	6	77	5	267	19	356	12
U	132	3	332	21	188	4	209	14	201	15	196	7
Ba/La_n	1·00	0·03	5·28	0·47	1·06	0·04	1·85	0·14	1·22	0·12	1·12	0·03
Th/La_n	1·00	0·03	2·40	0·27	1·11	0·04	0·42	0·04	0·94	0·10	1·15	0·05
Zr/Hf_n	1·00	0·06	0·54	0·05	0·82	0·04	0·57	0·06	0·66	0·09	0·73	0·06
Nb/Ta_n	1·00	0·06	0·78	0·07	1·06	0·08	0·90	0·07	0·91	0·13	0·90	0·10
Th/U_n	1·00	0·03	0·28	0·03	1·04	0·04	0·22	0·02	0·80	0·08	1·09	0·06

All analyses in ppm, measured using SIMS, given on a H_2O reintegrated basis; c15 = superliquidus experiment = starting material.
*Measured using EMPA.

Table 5: Trace element composition of experimental monazite and Macusani obsidian and calculated partition coefficients

Run:	c10		c23		c13		Macusani
°C:	800		850		800		650
Monazite:	$n=5$	1σ	$n=6$	1σ	$n=9$	1σ	
La	88500	10300	98600	3360	91100	15800	94700
Ce	87500	10300	97800	3850	92100	15400	207500
Nd	84800	7530	90600	4330	85300	12300	94600
Sm	52200	7520	47900	5310	34800	3610	20100
Eu	33400	7880	28700	4050	13700	1140	–
Gd	–	–	–	–	–	–	15000
Th	235300	59300	213200	26140	287100	49350	64000
U	18100	1440	15200	2430	35100	10590	20000
$D_{mon\text{-}melt}$							
La	1290	280	1080	70	700	130	78900
Ce	1320	310	1090	80	700	130	57600
Nd	1300	250	1070	70	740	110	–
Sm	970	200	820	90	620	70	39400
Eu	710	180	590	80	480	50	–
Gd	–	–	–	–	–	–	23800
Th	1320	360	820	110	3710	700	37600
U	63	6	56	9	170	50	980
$D_{Th/La}$	1·0	0·4	0·8	0·1	5·4	1·4	0·5
$D_{Th/U}$	23	7	16	3	24	9	38

Partition coefficients make use of H_2O-correction.

(e.g. Ganguly *et al.*, 1998; Van Orman *et al.*, 2002; Tirone *et al.*, 2005) and because garnet is known to have some very high and very low partition coefficients ($D_{grt/rock}$). Given that analyses were made on randomly cut garnets, single measurements will reflect various snapshots of the zoning profiles, which should produce scatter in the data. Indeed, SIMS analyses of garnets can have 1σ of up to 70% relative, and these are most marked for highly compatible (HREE) or incompatible (LREE) elements. Although these calculated partition coefficients are subject to relatively high errors, relative variation in element ratios will be considerably less (e.g. Wood *et al.*, 1999).

Garnet–melt partition coefficients are given in Fig. 10 and Supplementary Data File 4, and generally agree well with existing studies at similar conditions (e.g. Green *et al.*, 2000; Klimm *et al.*, 2008). It is evident that temperature strongly influences the partition coefficients, with $D_{grt/melt}$ decreasing with increasing temperature, consistent with Van Westrenen *et al.* (2001). Temperature dependence is more pronounced compared with chemical dependence, given that garnets with the lowest $X_{grossular}$ occur at the highest temperatures in this study (but $D_{grts/melt}$ generally increases with decreasing $X_{grossular}$, Van Westrenen *et al.*, 2001). HREE and Y are the most compatible, with D_{HREE+Y} generally ~200–300 at $T=800$–900°C, and ~50–100 at 1000–1100°C. Scandium has slightly lower D values of 80–140 at $T=800$–900°C, and ~20–50 at 1000–1100°C. Elements with D values around 1–10 include Ti, V, Zr, Hf, Sm, and Eu, all showing an overall small decrease with increasing temperature. Incompatible elements with $D<1$ were Li, Nb, Ta, Th, U, La and Ce. The most incompatible elements, with $D \leq 0{\cdot}01$ at all temperatures, are Ba and Sr. As explained above, garnet strongly fractionates LREE and LILE from HREE, and further causes small fractionation by preferring Zr over Hf (~2–3 times) and U over Th (2–3 times). Nb/Ta fractionation (~1) and Th/La fractionation are less well constrained by our experiments (~0·5–2), as a result of analytical imprecision.

Rutile–melt partitioning

Rutile–melt partition coefficients from six experiments are given in Supplementary Data File 5. D_{Nb} and D_{Ta} both vary from 900 to 200, with the highest D_{Nb} and D_{Ta} values at lowest temperatures. $D_{Nb/Ta}$ is consistently around unity (average $=1{\cdot}05 \pm 0{\cdot}08$). This is considerably higher than the $D_{Nb/Ta}$ of around 0·56 of Klimm *et al.* (2008) for basaltic fluids; however, both values agree well with the data of Schmidt *et al.* (2004*a*, e.g. Fig. 5), who showed that rutile–melt $D_{Nb/Ta}$ increases with increasing melt SiO_2. Ilmenite in our experiments was found to contain Nb and Ta well below the detection limits of EMPA at our applied conditions. We hence conclude that our ilmenites host insignificant amounts of Nb (and probably Ta), although they can be up to 10 times more modally abundant.

Monazite–melt partitioning

Monazite–melt partition coefficients are presented in Table 5 and Fig. 11. Calculations were hampered by several factors. First, monazite occurs in trace amounts and only a few grains were suitably large for analysis, problems that were exacerbated at higher temperatures because of reduced proportions of monazite. Second, many analyses exhibited non-stoichiometric amounts of REE + Th:P + Si owing to contamination by surrounding phases. Small amounts of contamination should not alter the REE + Th analysis because monazite is by far their major host, so we have confined ourselves to analyses with <10% contamination. Finally, monazites exhibit zoning, which makes analysis somewhat dependent on sectioning. Hence, only samples where enough grains were present to be analysed in detail are likely to be representative.

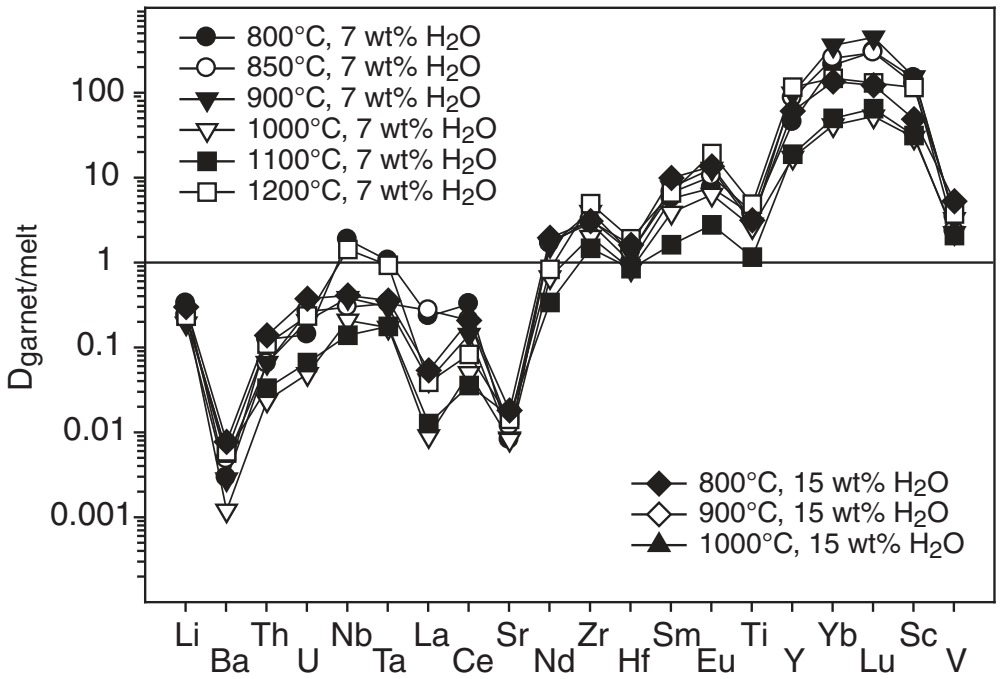

Fig. 10. Garnet–melt trace element partition coefficients from our experiments. Partition coefficients for LREE, HREE, and Th may be subject to high uncertainties (see text for discussion). Data from Supplementary Data File 4.

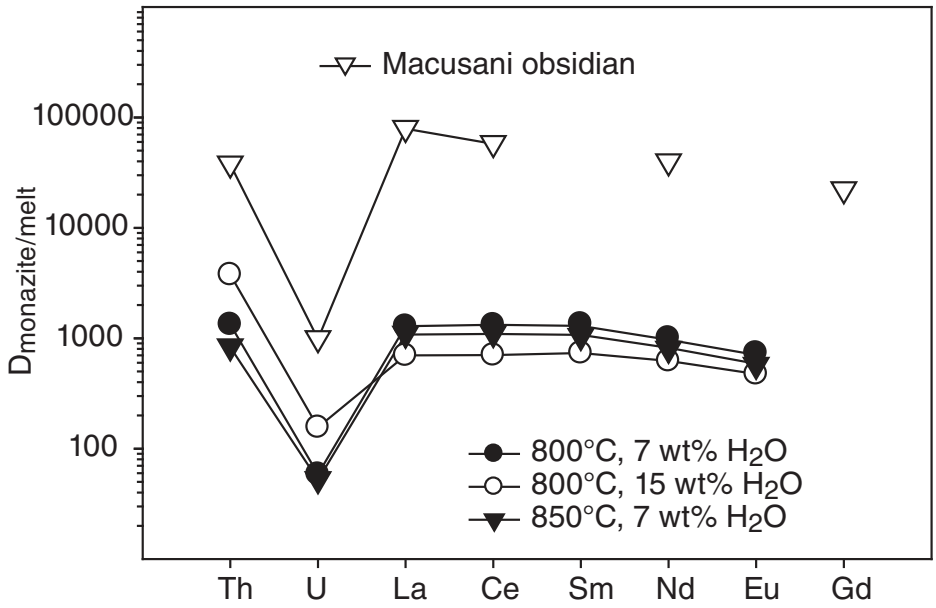

Fig. 11. Monazite–melt partition coefficients for LREE, U and Th from our experiments, compared with a natural monazite-bearing obsidian glass (Macusani, Peru; Pichavant *et al.*, 1987; Montel, 1993). Data from Table 5.

We have supplemented the partition coefficients determined from monazite analyses with values derived from mass balance, assuming that melt and garnet are the only other phases to accommodate U, Th and LREE. Both sets of values are given in Table 6. Where we have partition coefficients from both methods agreement is good and the overall partitioning patterns displayed in Fig. 12a and b are generally consistent with Fig. 11. The only exception is experiment c9, where the only two measurable grains of monazite were excessively Th-rich compared with

Table 6: Trace element composition of experimental monazite and monazite–melt partition coefficients via mass balance

	This study											
Run:	c10		c23		c9		c17		c13		c21	
°C:	800		850		800		800		800		900	
		1σ		1σ		1σ		1σ		1σ		1σ
Monazite												
La	113300	17000	159100	20700	194400	85500	121700	5630	114500	11600	210200	307700
Ce	114100	16700	165000	18100	189600	83300	121900	5390	113300	11600	131900	217800
Nd	108400	16900	133800	17200	128700	67300	114400	5900	113100	11400	–	–
Sm	65700	17700	21700	17800	–	–	69600	8680	48600	10200	–	–
Eu	54300	18900	–	–	–	–	60000	10600	–	–	–	–
Th	139800	33400	141700	18800	100900	115500	135800	9690	241100	14100	304100	501200
U	34100	52600	–	–	–	–	–	–	9600	17500	–	–
$D_{mon\text{-}melt}$												
La	1640	310	1740	250	1050	470	2640	240	880	100	1050	1540
Ce	1730	340	1850	230	1050	470	2690	220	870	100	680	1120
Nd	1670	300	1580	220	910	480	2450	190	980	110	–	–
Sm	1220	310	370	300	–	–	2050	310	870	190	–	–
Eu	1160	350	–	–	–	–	2750	540	–	–	–	–
Th	780	170	540	80	290	340	870	90	3130	280	1140	1910
U	120	150	–	–	–	–	–	–	50	80	–	–
$D_{Th/La}$	0·5	0·2	0·3	0·1	0·3	0·4	0·3	0·0	3·6	0·5	1·1	2·8
$D_{Th/U}$	6·5	17	–	–	–	–	–	–	68	45	–	–

	Hermann & Rubatto (2009)					
Run:	C1563	C1614	C1872	C1578	C1699	C1848
°C:						
Monazite						
La	121400	145600	103000	137200	113500	104900
Ce	48700	58600	42600	55600	46900	43100
Nd	34900	45900	30900	43500	34000	31800
Sm	28100	43800	25000	38700	27700	26500
Eu	7690	14000	9750	12600	10700	10800
Th	160800	194400	151600	174800	158600	152600
U	268900	155200	314000	198800	281000	306000
$D_{mon\text{-}melt}$						
La	890	790	1200	1210	1060	1360
Ce	810	750	1220	1160	1070	1310
Nd	780	880	1190	1400	1030	1450
Sm	720	1290	1000	1760	960	1560
Eu	240	560	410	740	410	770
Th	670	660	1300	880	790	1330
U	340	140	670	280	300	710
$D_{Th/La}$	0·7	0·8	1·1	0·7	0·8	1·0
$D_{Th/U}$	2·0	4·6	1·9	3·1	2·6	1·9

Partition coefficients make use of H_2O-correction (for this study).

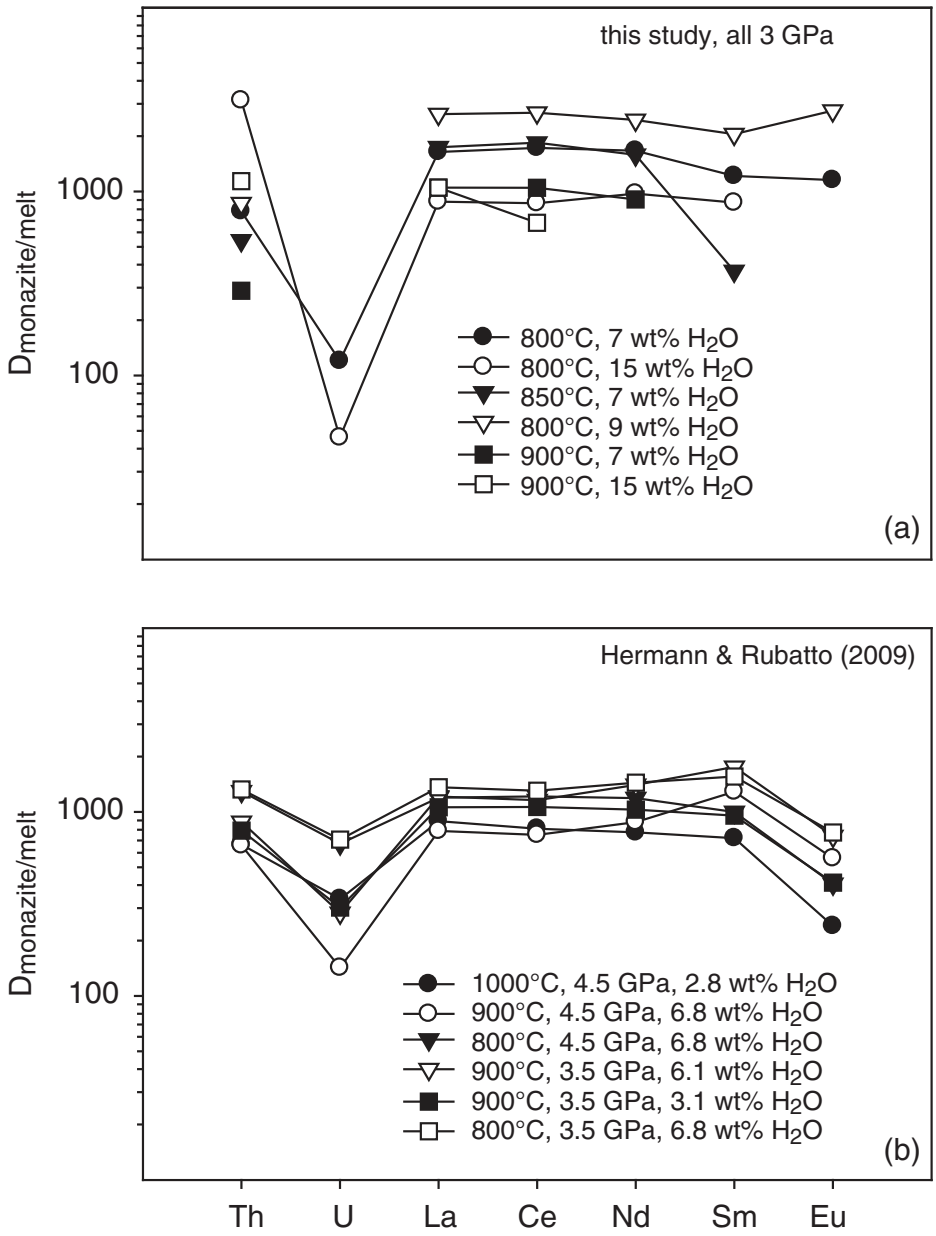

Fig. 12. Calculated monazite–melt partition coefficients for LREE, U and Th from (a) this study and (b) that of Hermann & Rubatto (2009), using a mass-balance approach. The latter experimental study involved very high U concentrations (>500 ppm) for which there may be additional hosts, for which we cannot account. (See text for details.) Data from Table 6.

mass-balance constraints. We believe that this discrepancy is related to chemical variability combined with the measured monazite not being representative for this sample. Indeed, some other monazites, for which measurements were contaminated (>l0%) by the surrounding matrix, appear to have much lower Th concentrations. It is clear that errors on mass-balance partition coefficients are significantly higher than those on measured values because of error propagation through the calculations (e.g. phase proportions, analytical), and this is most notable near monazite-out at ~900°C.

We have also tried to estimate the monazite composition for the dataset of Hermann & Rubatto (2009) by the same method. For garnet modal abundance, we have used 20% (J. Hermann, personal communication); garnet trace element contents of our run c10 were used for all of their garnets. Meaningful error propagation could not be performed. It should be noted, however, that the exact trace

content of garnet is largely insignificant for our mass balance as the key elements (La, Th) will primarily be hosted by monazite and melt.

Calculated and measured monazite–melt partition coefficients (Figs 11 and 12a,b) reveal, as expected, that LREE + Th are strongly retained in monazite compared with the melt phase, especially at low temperatures. Also, monazite fractionates La from heavier REE (e.g. Sm), with D_{La}/D_{Sm} varying from 1·1 to 1·3. Water-rich melts can dissolve more LREE + Th compared with water-poor melts (e.g. Rapp & Watson, 1986), reflected in lower bulk D_{LREE} for 800°C when 15 wt % H_2O was loaded in the experiment compared with 7 wt %. All monazites strongly fractionate Th from U, with D_{Th} 16–24 times greater than D_U. $D_{Th/La}$ varies widely, from ~0·3–5. In Fig. 11 we further compare our partition coefficients with those of a natural monazite–rhyolite glass pair from Macusani, Peru (Pichavant *et al.*, 1987; Montel, 1993). The calculated equilibrium temperature for the Macusani rhyolite is ~650°C (Pichavant *et al.*, 1987) at a sub-volcanic pressure of ~200 MPa. As expected, partition coefficients for LREE and Th are much higher than those in this study, because of the strong temperature dependence of monazite solubility. However, the overall pattern is similar, with $D_{Th} > D_U$ and $D_{La} > D_{Sm}$. It is striking that at Macusani $D_{Th}/D_{La} = 0·5$, further supporting our observation that this ratio is not necessarily unity (see Plank, 2005; Hermann & Rubatto, 2009).

Natural monazites are a solid solution of monazite [$LREEPO_4$], huttonite [$ThSiO_4$] and brabantite [$Ca_{0·5}Th_{0·5}PO_4$], and the relative solubilities of these three components may play a role in controlling the relative partitioning of LREE and Th. This is more acute in doped experiments, where LREE/Th ratios are typically much higher than they are in nature. For example, we observe that in most cases $D_{La}/D_{Th} < 1$ (Fig. 11), except for one experiment with high water content (c13: 800°C, 15 wt % H_2O) where $D_{La}/D_{Th} \sim 5$. We believe that this may be due to different solubility behaviours of Th vs LREE end-members of monazite solid solution as a response to increased water contents (see Supplementary Data File 6 for more information).

Melt–bulk solid partitioning

Partition coefficients between the bulk residue and melt can be calculated from the glass fraction determined by mass balance and the compositions of the starting material and the glass (Fig. 13a), with the caveat that fluid-corrected trace element concentrations, together with mass-balance uncertainties, may be subject to relatively high errors. Indeed, if trace elements are predominantly in the melt phase, mass balances for solids can be within error of zero. We therefore consider only solid–melt partition coefficients between 0·01 and 100. Partition coefficients are shown in Fig. 13, and given in Supplementary Data File 7.

The most incompatible (or fluid-mobile) element, which is not retained to any significant degree in the solid residue at any temperature, is Sr (see Hermann & Rubatto, 2009). Hermann & Rubatto (2009) have also noted that Cs (not present in our experiments) is similarly incompatible. Barium is also highly incompatible, but partly held back by phengite (e.g. Hermann, 2002) up to ~850°C. U and Li are also relatively fluid-mobile. Elements that are buffered by accessory phases (rutile: e.g. Ryerson & Watson, 1987; monazite: Rapp & Watson, 1986; zircon: Watson & Harrison, 1983) have strongly increasing $D_{melt/solid}$ with increasing temperature as a result of increased solubilities up to the point that the host phase becomes exhausted. This is most notable for LREE and Th (monazite-buffered, exhausted above ~900°C), and Ti, Nb and Ta (rutile-buffered, exhausted above ~1000°C). In the case of monazite control we illustrate this behaviour in Fig. 14a and b, where the La and Th contents of melts are plotted versus melt fraction and temperature, respectively, for 7 wt % and 15% H_2O. Both La and Th increase to maximum values at the point of monazite exhaustion, plotting thereafter along a dilution curve consistent with D_{La} and D_{Th}, both being approximately zero. This trend corresponds well to either positive monazite identifications or inferences from mass balances at any given temperature (Fig. 14b). The different melt fractions at which monazite is exhausted are clear from the displaced maxima between the 7% and 15% H_2O series. Similar behaviour is observed for rutile control of Nb and Ta (Fig. 14c and d). Similar conclusions cannot be drawn for Zr and Hf (Fig. 14e and f); because of appreciable incorporation of these elements into residual garnet (Fig. 10), zircon-out as suggested by mass balance ($T \sim 850$°C) does not correspond to the maxima in a concentration versus melt fraction or temperature diagram (Fig. 14e and f). In all three panels of Fig. 14 it is clear from the displacement of the curves for 7% H_2O and 15% H_2O that H_2O, as well as temperature, exercises a strong control on the solubilities of monazite, rutile and zircon (see Rapp & Watson, 1986, for monazite; Xiong *et al.*, 2009, for rutile).

The fact that monazite fractionates Th from La means that the source-normalized Th/La ratio of the fluids is not unity until the point of monazite exhaustion. Our values differ somewhat from those of Hermann & Rubatto (2009), who found that $D_{Th/La}$ in monazite-saturated experimental melts lay close to unity over a wide temperature range. However, their initial doping levels differ significantly from ours in having higher Th (and U) relative to LREE.

Effects of doping

Before considering the implications of our experimental results for trace element behaviour during melting of natural

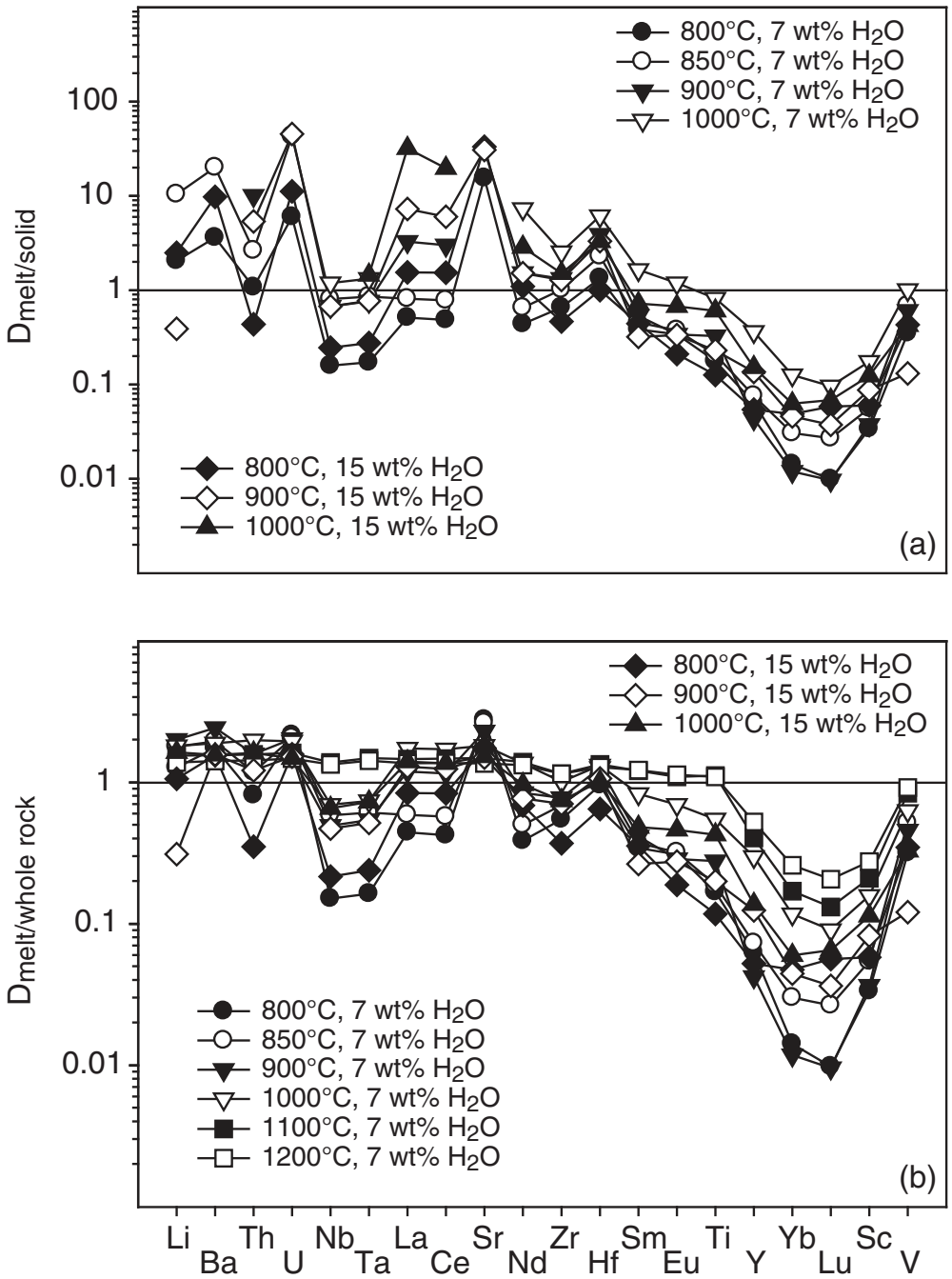

Fig. 13. (a) Melt–bulk solid and (b) melt–whole-rock partition coefficients from this study, using the H_2O reintegrated modal proportions from Table 2 and corrected glass analyses from Table 4. Data from Supplementary Data File 7.

radiolarian clay it is important to consider the effects of doping the starting materials with some trace elements in excess of natural values. This practice is widespread in experimental studies of trace element behaviour to generate sufficient accessory phases to be positively identified in run products. It is, however, clear from Fig. 14 that the presence or absence of accessory phases can, in fact, be deduced in many cases from the evolution of trace elements with increasing melt fraction without the need to dope.

The elements most affected by doping levels are those that are major structural components of accessory phases.

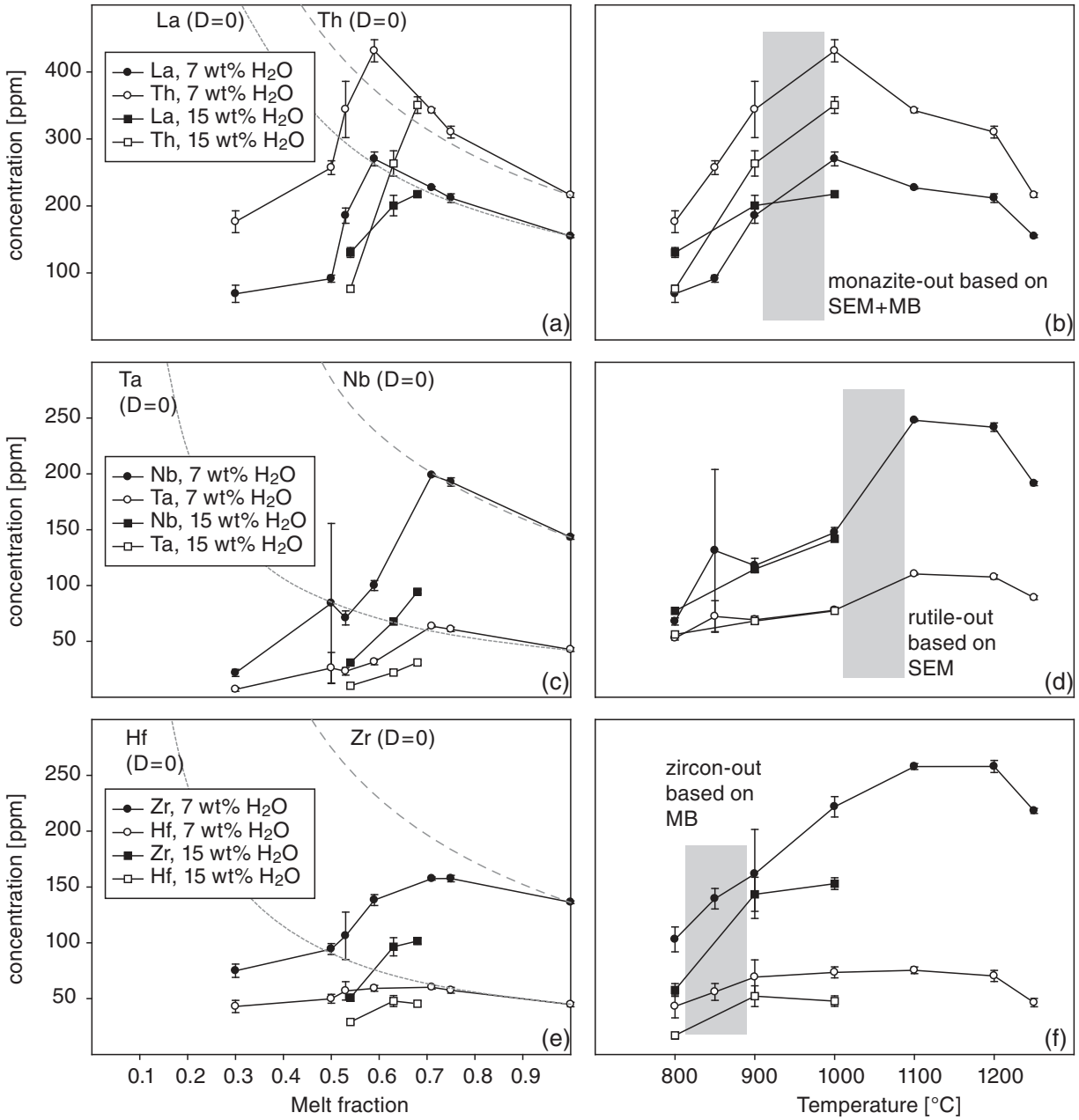

Fig. 14. (a–f) Concentrations of various trace elements in the melt, which are principally controlled by accessory phase solubilities (La, Th = monazite; Nb, Ta = rutile; Zr, Hf = zircon), plotted against melt fraction (a, c, e) and temperature (b, d, f). Trace element concentrations steadily increase until the point of host phase exhaustion. This is indicated in (a), (c) and (e) where trace elements start following a trend as predicted by $D = 0$ (= exhaustion), and in (b), (d) and (f) by decreasing concentrations (see Klemme *et al.*, 2002). These trends are in agreement with either positive identification of host phases via SEM or mass balance (MB). Zircon-out is not well matched because of the persistence of garnet, which hosts significant amounts of Zr ± Hf.

The principal effect of doping is to increase the modal amount of an accessory phase. Although this does not affect the solubility of the phase (within reasonable limits) it does affect the bulk partition coefficient for additional trace elements that are incorporated into that phase. Klimm *et al.* (2008) discussed the case of rutile. They showed that adding additional TiO_2 to a starting material does not affect Ti solubility (and hence TiO_2 in the melt), but does affect the bulk partitioning behaviour of Nb and Ta because it is related to the modal abundance of rutile via $D_{Nb}^{bulk} = X_{ru} \times D_{Nb}^{ru}$ (or $D_{Ta}^{bulk} = X_{ru} \times D_{Ta}^{ru}$) where X_{ru} is the modal abundance of

rutile. It is therefore very important to acknowledge the distinction between solubility (unaffected by doping) and bulk partitioning (affected by doping) (see Hanson & Langmuir, 1978).

Our experimental starting materials have Ti and Zr contents similar to natural radiolarian clay (Table 1) therefore the modal abundance of rutile and zircon in our experiments mimics that in nature. Consequently the bulk partitioning behaviour of trace elements preferentially taken up into these phases (Nb, Ta, Hf) will be unaffected and the doping issue need be considered no further. In the case of monazite the situation is more complex because monazite exhibits extensive solid solution between three end-members containing LREE and/or Th: monazite ($LREEPO_4$), huttonite ($ThSiO_4$), and brabantite ($Ca_{0.5}Th_{0.5}PO_4$). Thus in systems doped with high levels of Th, relative to LREE, Th may become a major (or 'essential') structural component. In our experiments both Th and LREE are added in excess of natural levels (Table 1), such that Th/LREE is nearly four times higher than in natural radiolarian clay. [Th/LREE of Hermann & Rubatto's (2009) starting material is over six times higher]. As a consequence our experimental monazites are solid solutions with appreciable huttonite and brabantite components (Fig. 9). (Analogously, coffinite may become a major structural component in monazite in experiments that are highly doped in U, although other phases such as garnet and zircon can host significant amounts.) As all components are likely to display solubility dependences on temperature, pressure and composition (including H_2O) that differ from those of monazite, and may exhibit non-ideal interactions in monazite solid solutions, it is plausible that the behaviour of Th, U and other LREE in our experiments (Fig. 14) does not replicate that in nature.

The transition from partitioning-controlled behaviour, where a species acts as a passive trace component, to solubility-controlled behaviour, where the species becomes a major structural component, corresponds thermodynamically to the change from Henry's Law behaviour to Raoult's Law behaviour (separated by a transitional zone). In most magmatic systems a species can be considered as showing one or other type of behaviour. For example, in the case of rutile, Ti is Raoultian, whereas Nb and Ta are Henrian. For natural rocks where La (and other LREE) are much more abundant than Th (and U), one would imagine that La is Raoultian, whereas Th is Henrian. It is possible, however, that in systems doped with significant Th, such as ours and that of Hermann & Rubatto (2009), one may see the transition from Henrian to Raoultian behaviour. This transition must be accounted for if experimental data are to be applicable to nature.

The solubility of a component, say huttonite, in a fluid or melt (hereafter just 'fluid') can be described by an equilibrium constant, K_{sol}^{hut}:

$$K_{sol}^{hut} = \frac{\alpha_{mzss}^{hut}}{\alpha_{fluid}^{hut}} = \left(\frac{\gamma_{mzss}^{hut}}{\gamma_{fluid}^{hut}}\right) \times \frac{X_{mzss}^{hut}}{X_{fluid}^{hut}} = f(P,T,X) \qquad (1)$$

where mzss denotes monazite solid solution, α denotes activity, γ denotes the activity coefficient and X denotes molar fraction. An analogous expression can be written for LREE in mzss. In the Raoult's Law region, where $\alpha = X$, the γ terms are unity. Thus the Th (and LREE) content of the fluid at a given pressure, temperature and fluid composition depend inversely on the monazite solid solution composition. For binary huttonite–LREE monazite solid solutions the weight fraction Th in mzss is given by

$$Th_{mzss} = \frac{232.04 X_{mzss}^{hut}}{233.88 + 90.25 X_{mzss}^{hut}} \qquad (2)$$

and the molar fraction of Th in the fluid can be calculated from the molar fraction of all other cations in the fluid. For a given fluid composition

$$Th_{fluid} = c X_{fluid}^{Th} \qquad (3)$$

where the constant of proportionality, c, is related to the gram formula weight of the fluid. Equations (1)–(3) can be combined to yield the effective Nernst partition coefficient in the Raoult's Law region (D_{Th}^{Raoult}) at a given P and T:

$$D_{Th}^{Raoult} = \frac{Th_{mzss}}{Th_{fluid}}. \qquad (4)$$

In the Henrian region, at the same P and T, the partition coefficient is a constant:

$$D_{Th}^{Henry} = \frac{Th_{mzss}}{Th_{fluid}} = \text{constant}. \qquad (5)$$

Henrian behaviour applies when $X_{mzss}^{hut} \rightarrow 0$ and the Raoultian region when $X_{mzss}^{hut} \rightarrow 1$. Between these two terminal regions there is a transition, whose form depends on the ratio of the activity coefficients $\gamma_{mzss}^{hut}/\gamma_{fluid}^{hut}$. According to the Gibbs–Duhem relationship, when Th shows truly Raoultian behaviour, the LREE are Henrian and vice versa. In Fig. 15 we show this behaviour schematically for D_{Th} and D_{LREE}. The ratio of D_{Th}/D_{La} is a sensitive function of monazite solid solution, which depends on the doping levels of these two elements. The behaviour of natural systems, where LREE $\gg$ Th, is likely to approximate that in which Th is Henrian and the LREE (La) are Raoultian, whereas in doped systems, where Th $\sim$ LREE, Th and LREE (La) may enter the transitional region.

Unfortunately, quantitative assessment of this model is hampered because of our limited and unsystematic (polythermal, polybaric) datasets; however, we can qualitatively

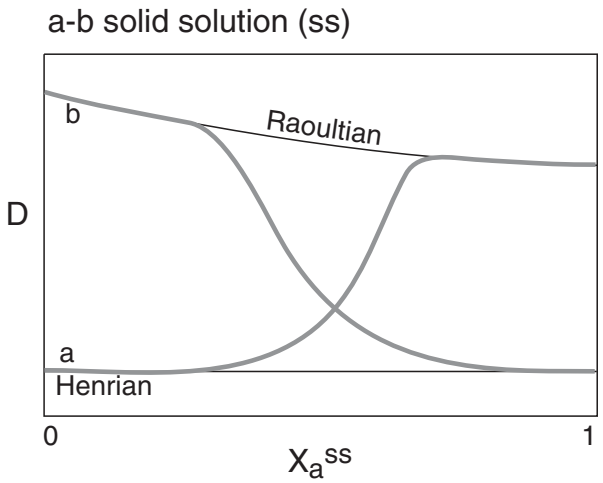

Fig. 15. Schematic diagram illustrating the partitioning behaviour of elements *a* and *b* that form a solid solution (ss), as a function of X_a^{ss}. Behaviour depends on the relative concentrations of *a* and *b*: if $a \ll b$, then *a* shows Henrian behaviour whereas *b* shows Raoultian behaviour, and vice versa. Transitional behaviour is expected for $a \approx b$.

assess its applicability by comparing calculated $D_{\Sigma LREE}$ and D_{Th} as a functions of X_{Th}^{mzss}. Figure 16 shows that $D_{\Sigma LREE}$ decreases with increasing X_{Th}^{mzss}, but this pattern is reversed for D_{Th}, consistent with our simple thermodynamic evaluation in Fig. 15. This suggests that both experimental studies [this study and that by Hermann & Rubatto (2009)] have investigated partitioning behaviour that is entering the 'transitional zone' as defined above, where results are sensitive to doping levels. Our data span a larger range in partitioning behaviour when compared with the dataset of Hermann & Rubatto (2009), which may be attributable to greater solubility differences between monazite and huttonite at the very high H_2O contents in some of our experiments. We have contoured the experimental data for D_{Th}/D_{La} in Fig. 16b (change from $D_{Th} < D_{La}$ to $D_{Th} > D_{La}$ with increasing X_{Th}^{mzss}), to determine whether Th will be fractionated from La in the presence of monazite in natural radiolarian clay. In the absence of reliable partitioning data, X_{Th}^{mzss} can be estimated only for sub-solidus conditions, assuming that the sub-solidus monazite composition has an LREE/Th ratio close to that of the bulk-rock (i.e. monazite is the only major LREE + Th host). Figure 16b shows that monazites from natural radiolarian clay are likely to have a very small X_{Th}^{mzss} of $< 0{\cdot}1$, which plots in the area where our experiments show $D_{Th} < D_{La}$. This is consistent with our natural example (Macusani Obsidian), whose X_{Th}^{mzss} also plots in that range. Based on the available data we therefore conclude that doping does affect the relative partitioning of Th and La and that, for natural levels of Th and La, $D_{Th}/D_{La} < 1$. Such a value may generate Th–La fractionation in fluids relative to their solid residues.

DISCUSSION

Melting behaviour of subducting sediments

The experiments in this study were performed assuming that external water is available during melting; for example, as a result of serpentinite breakdown from the underlying portions of the slab. Fluid-present melting of subducted sediments has been suggested previously (e.g. Domanik & Holloway, 1996), and high-pressure phase relations in S-type granites (broadly similar to clays) with different water contents were determined by Huang & Wyllie (1973, 1981). Excess water in our experimental study ranges from 6·5 to 14·5 wt %, given that, for the bulk radiolarian clay composition, only ~0·5 wt % of water (total) would be structurally bound up in sub-solidus phengite. Our experiments show that substantial volumes of melt can be generated above the solidus if excess, externally derived water is available. Melt fractions (F) could be >0·5 even at near-solidus temperatures (~800°C) if around 15 wt % water is available at 3 GPa. Our attempt to perform fluid-absent experiments (~1 wt % H_2O) failed because no detectable reaction occurred in our starting material, even at temperatures ≥900°C.

In Fig. 17 we compare our results to those of Schmidt *et al.* (2004*b*) for a greywacke and a pelite, the latter being chemically similar to radiolarian clay. Figure 17 illustrates clearly that, for an overstepping of $T_{solidus}$ of ~50°C, only negligible amounts of melt ($F < \sim 0{\cdot}1$) would be generated if no (or negligible) external fluid is available. Figure 17 further shows that substantial melting ($F > 0{\cdot}5$) in fluid-absent systems can be achieved only at relatively high temperatures (~1000°C) where phengite disappears [see also discussion by Hermann & Spandler (2008)]. In fact, the melt fraction in our study at phengite-out (~830–870°C) approximately equals the phengite-out melt fraction of Schmidt *et al.* (2004*b*) at ~1000°C (Fig. 17). Differences in detail are probably related to the starting composition, especially the amount of K_2O, stabilizing different amounts of phengite.

We can model the observed differences between fluid-absent and fluid-excess melting behaviour in terms of a simple binary between an anhydrous aluminosilicate component (in the case of end-member phengite, this is orthoclase + orthopyroxene) and pure H_2O, wherein phengite is an incongruent-melting, intermediate compound (Fig. 18). Our schematic phase diagram is calculated for the case where the 'fluid' lies just below the second critical end point, such that there is a eutectic between phengite and H_2O (see Kessel *et al.*, 2005*b*). We use the schematic phase diagram to calculate melt productivity (F–T) paths for three contrasted scenarios: fluid-absent melting of phengite (A), melting with a very small amount of excess fluid (B) (see Schmidt *et al.*, 2004*b*), and melting with substantial excess fluid (C + D), approximating that in our experiments. We show that the calculated F–T curves bear

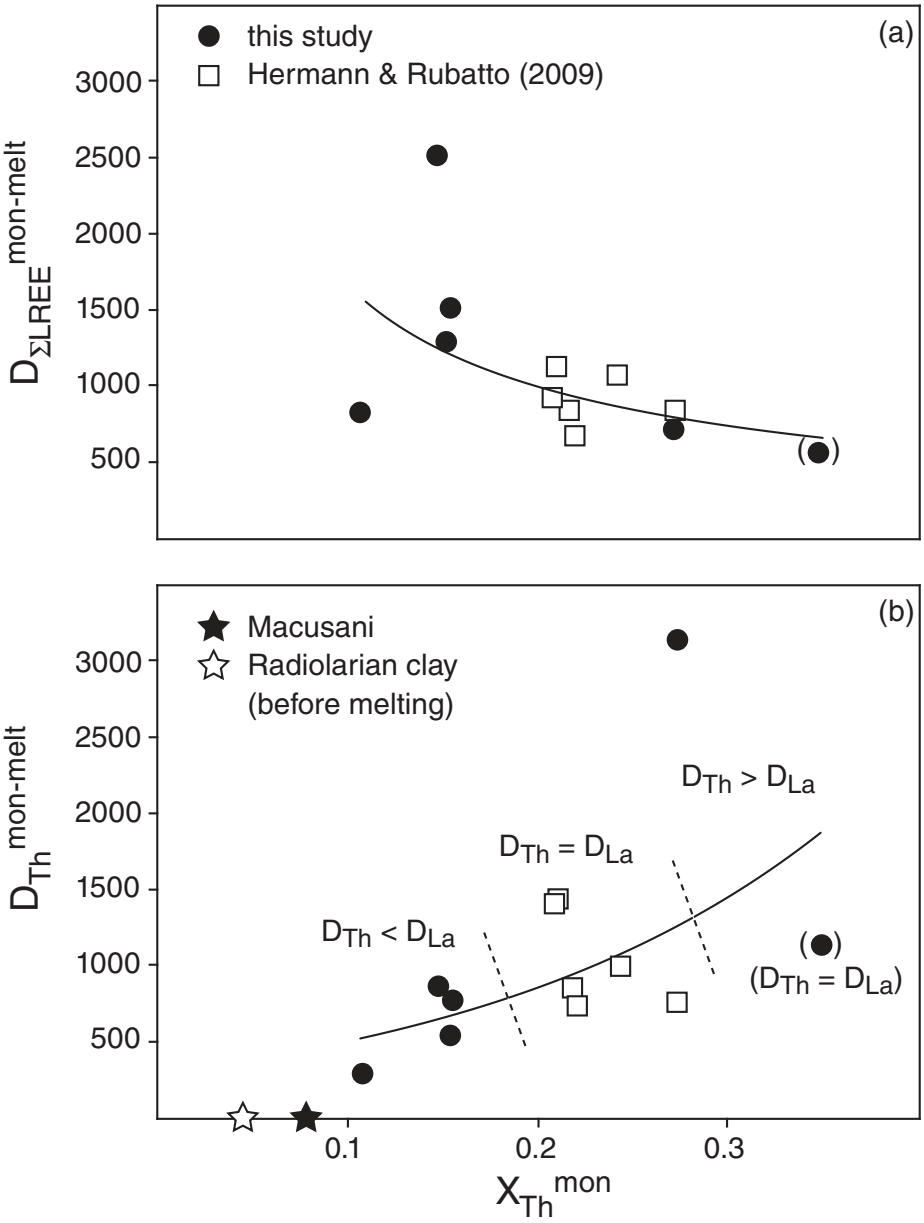

Fig. 16. Partitioning behaviour of ΣLREE (a) and Th (b) between monazite and melt as a function of X_{Th}^{mon}. Whereas $D_{\Sigma LREE}$ decreases with increasing X_{Th}^{mon}, D_{Th} shows the opposite behaviour. This pattern is consistent, in principle, with the simple thermodynamic evaluation in Fig. 15. Continuous lines are eyeball fits. Also shown in (b) are contours of D_{Th}/D_{La} as well as estimated X_{Th}^{mon} of natural radiolarian clay, suggesting that, in nature, Th will be fractionated from La in the presence of monazite. (Note that the presence of monazite in the experiment marked with brackets is uncertain based on mass balance).

similarities to those depicted in Fig. 17, with maximum melt production achieved at the point of phengite breakdown, which occurs at lower T in scenarios (C) and (D), compared with (A) and (B). Of course, natural sediments are not peritectic binaries, because of ubiquitous solid solution and the presence of minor components. However, our simple approach illustrates clearly why melt productivity is negligible for fluid-absent (or fluid-poor) conditions except at high temperatures, whereas it is copious for the fluid-abundant case.

We conclude that dissolution of phengite ultimately controls melt productivity at high pressures (see Schmidt *et al.*, 2004*b*) and that this is considerably enhanced by the addition of water, even at relatively low temperatures. Hence, substantial volumes of melt can be generated close to the solidus if external water is available. In the absence

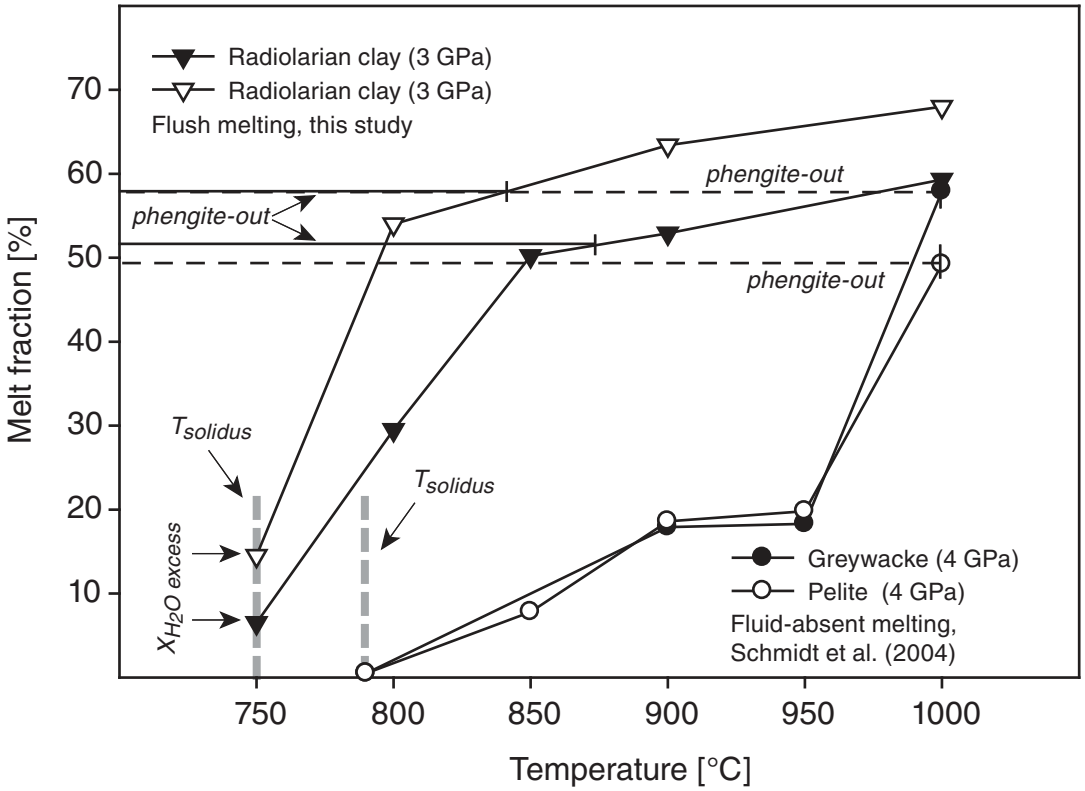

Fig. 17. Comparison of melt productivity (melt fraction %) in near fluid-absent melting experiments of Schmidt *et al.* (2004*b*) at 4 GPa, compared with melting of sediments in the presence of larger quantities of excess water (termed 'flush melting', this study, 3 GPa). Differences in $T_{solidus}$ include a pressure effect.

of such external fluids sediment would be (nearly) refractory at similar temperatures. There is clearly an important distinction between fluid-absent melting and what we term 'flush melting'.

Trace element signature of the melt

It is now well established that the presence or absence of trace element-rich accessory phases (e.g. rutile, allanite, monazite) is collectively responsible for the arc magmatic geochemical signature. The stability of rutile exerts primary control on the behaviour of HFSE (e.g. Brenan *et al.*, 1994; Foley *et al.*, 2000; Zack *et al.*, 2002; Klemme *et al.*, 2005); mirrored in arc volcanic rocks by negative Nb and Ta anomalies (e.g. Pearce & Cann, 1973; McCulloch & Gamble, 1991; Hawkesworth *et al.*, 1993; Thirlwall *et al.*, 1994). This characteristic is readily reproduced in this study (Fig. 13a and b), because rutile is present until ~1000–1100°C. Garnet is known to be a major host for the HREE (e.g. Stalder *et al.*, 1998; Van Westrenen *et al.*, 1999; Green *et al.*, 2000; Pertermann *et al.*, 2004) and is present up to the liquidus in our experiments. Zircon, as well as garnet, exercises further control on Zr and Hf, which may also show negative anomalies in arc magmas. However, the relatively early exhaustion of zircon from the residue means that appreciable Zr and Hf anomalies, above and beyond those attributable to garnet, would not be anticipated where the slab temperature exceeds ~850°C.

The behaviour of LREE + Th is controlled by the presence of residual allanite in subducted metabasalt, and potentially in some CaO-rich metasediments (Hermann, 2002; Klimm *et al.*, 2008), and by monazite in low-CaO metasediments (this study; Hermann & Rubatto, 2009). Allanite may also be present in metasediments as a low-*P* precursor of monazite (e.g. Hermann & Rubatto, 2009). Apatite may further be present in high-P_2O_5 protoliths (e.g. Johnson & Plank, 1999), but appears to contain too little LREE + Th to be of major significance [despite its abundance; see, e.g. Krenn *et al.* (2009) for trace element contents of coexisting apatite and monazite in UHP metapelites].

Plank (2005) has shown that for most arc magmas the magmatic Th/La ratio matches that of the subducted sediment associated with a particular arc. She argued that monazite does not appreciably fractionate Th from La at sub-arc conditions, a conclusion supported by Hermann & Rubatto (2009). Conversely, we have shown that Th–La fractionation in experiments is a sensitive function of

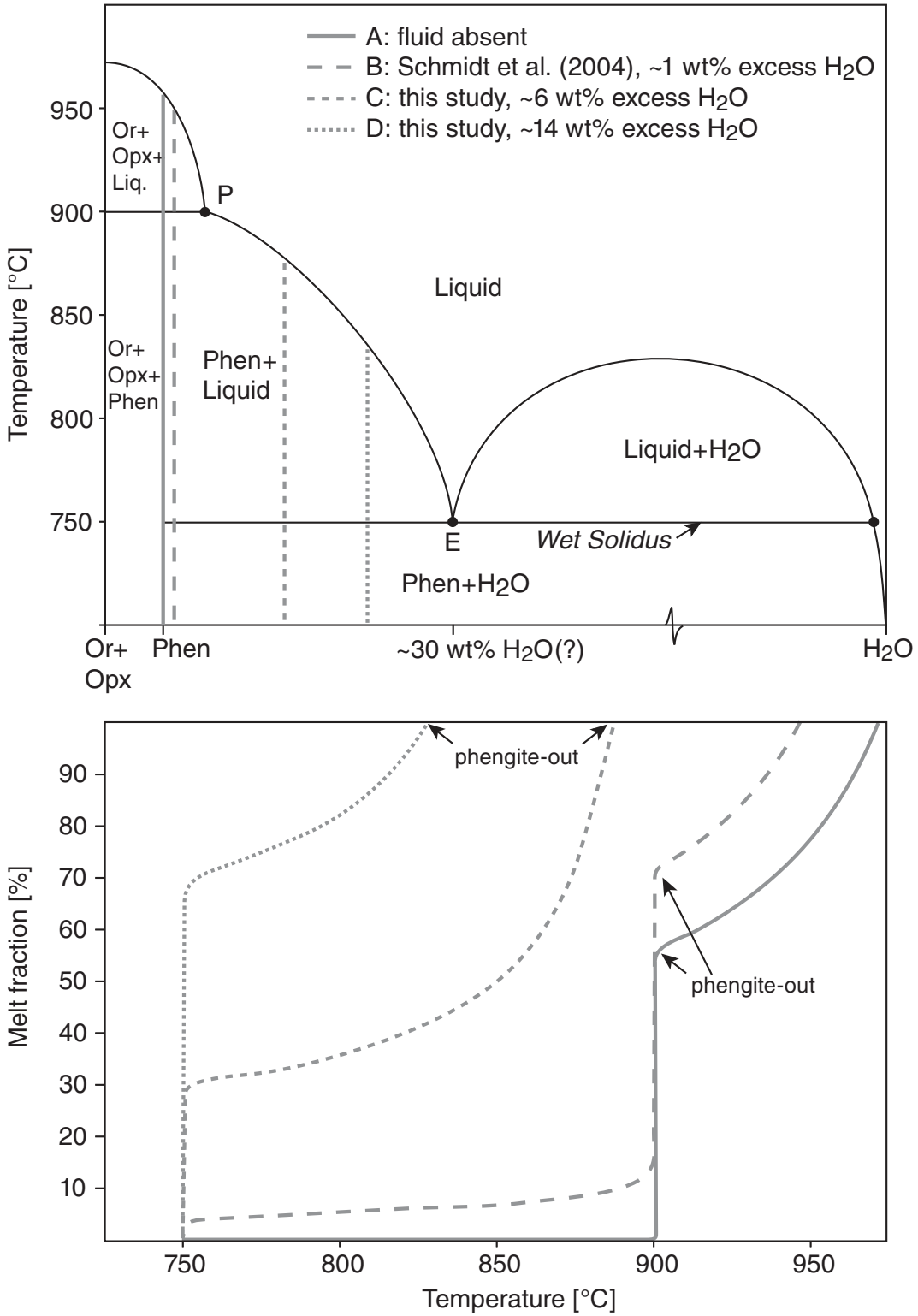

Fig. 18. Model melting behaviour in a simple, fictive binary system [orthoclase (Or) + orthopyroxene (Opx)–H_2O], where phengite [(Al)celadonite] is an intermediate phase, for bulk compositions corresponding to fluid-absent, 1 wt % excess H_2O (Schmidt *et al.*, 2004*b*), 6 wt % excess H_2O and 14 wt % excess H_2O.

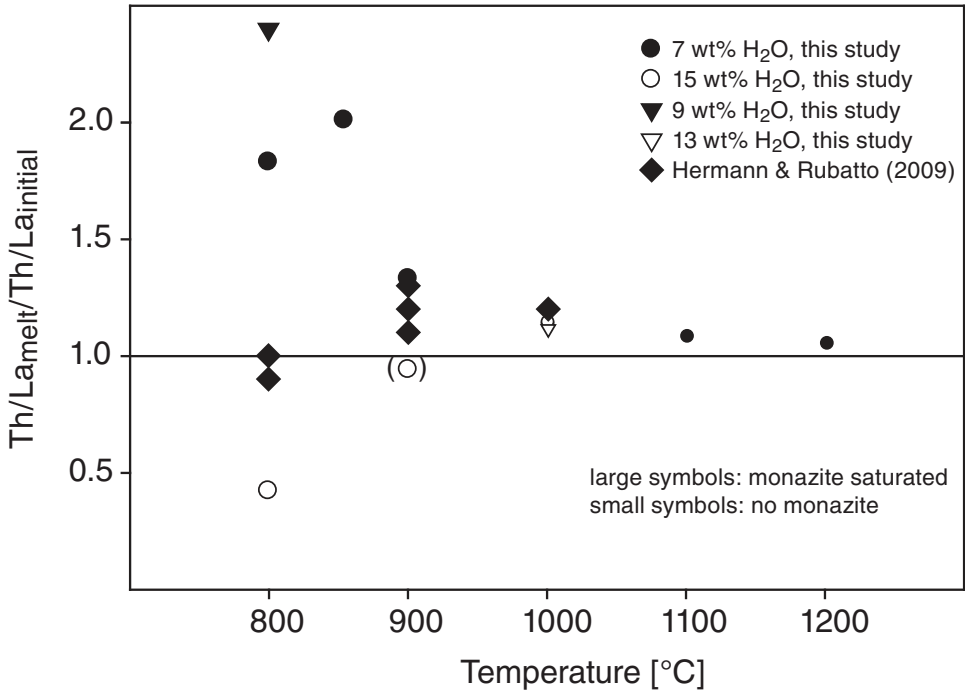

Fig. 19. Source-normalized Th/La_n as a function of temperature from our experimental study, compared with data from Hermann & Rubatto (2009). (Note that the presence of monazite in the experiment marked with brackets is uncertain based on mass balance).

doping levels of Th relative to LREE and that for realistic, low-Th sediments the effective D_{Th}/D_{La} ratio is probably significantly below unity. We conclude that Plank's (2005) observation is most simply reconciled with the destruction of monazite beneath most arcs. Of course, the monazite-out temperature is itself controlled by doping levels and must be extrapolated from the experiments (with ΣLREE ~ 788) to the natural situation [with ΣLREE ~ 177 after Plank & Langmuir (1998); Pr was not given but is estimated to be around 15 ppm]. Our experiments show that monazite solubility is a sensitive function of temperature and fluid composition (especially H_2O). We can use our measured solubilities for the series of experiments at 7 and 15 wt % H_2O to calculate the temperature at which monazite-out would occur for a radiolarian clay with natural LREE levels. At 7 wt % H_2O monazite-out is at ~840°C, whereas for 15% H_2O it is at ~780°C (see Supplementary Data File 8 for more information on the calculations). These can be considered approximate lower bounds for slab-top temperatures at sub-arc depths where radiolarian clay is a key subducting lithology.

The supply of LREE to volcanoes behind arcs, for example in back-arc basins (see, e.g. Portnyagin *et al.* 2007), appears to be inconsistent with complete destruction of monazite in the sedimentary portion beneath the arc, which would effectively relinquish all LREE. One solution is that monazite is not entirely destroyed beneath the arc, allowing tiny amounts of monazite to be carried beyond. Source-normalized Th/La ratios at near monazite-out will be close to their initial value, because bulk fractionation is a function of the modal amount of host accessory phase ($D^{bulk}_{LREE} = X_{mon} \times D^{mon}_{LREE}$ and $D^{bulk}_{Th} = X_{mon} \times D^{mon}_{Th}$). Hence, as $X_{mon} \rightarrow 0$, little bulk fractionation occurs even when $D_{Th}/D_{La} \neq 1$. This effect is apparent from a plot of source-normalized Th/La versus temperature (Fig. 19), where Th/La approaches unity at 900°C, although monazite is still present in tiny amounts at that temperature. Alternatively, back-arc LREE+Th could be supplied from the basaltic portion of the oceanic crust through the destruction of allanite at greater depth. Across-arc isotopic studies (e.g. Nd) would be required to quantitatively assess this possibility.

The study of Hermann & Rubatto (2009) shows that residual phengite controls the behaviour of LILE (e.g. K, Ba, Rb, Cs) (e.g. Domanik & Holloway, 1996; Schmidt, 1996; Sorensen *et al.*, 1997; Melzer & Wunder, 2000; Zack *et al.*, 2001; Hermann, 2002; Schmidt *et al.*, 2004*b*; Hermann & Rubatto, 2009). In our study phengite disappears at $T > 850$°C in runs with 7 wt % H_2O, and >800°C in runs with 15 wt % H_2O. Hermann & Rubatto (2009) have demonstrated that in the presence of phengite, fractionation of Rb from Cs occurs (which cannot be shown here because we did not add either of these elements), consistent with what is observed in nature

(Melzer & Wunder, 2000; Hermann & Rubatto, 2009). Hence, LILE fractionation is ensured by our experimental results until ~870°C, and this may represent an upper temperature limit for slab-top temperatures beneath, for example, the Lesser Antilles, provided that there is no phlogopite formation in the overlying mantle column (Wunder & Melzer, 2003). Moreover, in natural sediments Ba will not be significantly fractionated from La when both monazite and phengite are exhausted.

Implications for U/Th disequilibria

Our conclusions on monazite-free (or very monazite-poor) solid residues have implications for U/Th disequilibria in arc magmas (Avanzinelli *et al.*, 2008). A striking feature of many lavas from sediment-poor arcs is that they show a ^{238}U excess over ^{230}Th compared with their source, in contrast to sediment-rich arcs, which appear to plot close to the ($^{238}U/^{232}Th$) vs ($^{230}Th/^{232}Th$) equiline (e.g. McDermott & Hawkesworth, 1991; Condomines & Sigmarsson, 1993). The creation of excess ^{238}U in depleted arc lavas is generally explicable by the presence of either monazite or allanite in the dehydrating mafic crust (e.g. Hermann, 2002; Klimm *et al.*, 2008; Hermann & Rubatto, 2009; this study), which strongly retains Th in preference to U (Fig. 11). This leads to the development of a strong ^{238}U excess signal that may persist in young arc lavas that receive minimal sediment input. All samples, whether coming from sediment-poor or sediment-rich arcs, that plot on the ($^{238}U/^{232}Th$) vs ($^{230}Th/^{232}Th$) equiline can potentially be explained by having decayed back to equilibrium. A portion of the samples that plot close to the ($^{238}U/^{232}Th$) vs ($^{230}Th/^{232}Th$) equiline have minor ^{230}Th excesses (e.g. Condomines & Sigmarsson, 1993; Elliott *et al.*, 1997) that cannot be explained by decay alone. Only fluids or melts that have initially started with excess Th (compared with the initial composition) can plot above the equiline. Fluids or melts with excess Th, however, cannot be expelled in the presence of monazite because of strong retention of Th (compared with U) in monazite. Conversely, fluids or melts expelled from a monazite-free but garnet + rutile ± zircon-bearing solid residue will have excess Th, as a result of the strong preference for U over Th in these minerals (e.g. Blundy & Wood, 2003; Klemme *et al.*, 2005; Rubatto & Hermann, 2007). Hence, our proposal for a monazite-free solid residue is corroborated by U–Th disequilibria studies, and is consistent with a recent appraisal of the Marianas arc (Avanzinelli *et al.*, 2008).

CONCLUSIONS

We have shown that substantial melting of the subducted sedimentary layer can be achieved if external water is available, even at low, near-solidus temperatures. In contrast, fluid-absent melting produces negligible amounts of melt at similar temperatures. Water is also the key for the removal of monazite from the solid residue beneath arcs, given that such substantial melt volumes are capable of accommodating the entire LREE + Th budget of the subducting sediments. Arc genesis in the absence of residual monazite is supported by several geochemical features (Th/La; U/Th disequilibria) that have been reported from volcanic arcs worldwide.

The availability of water at sub-arc depths appears to be the key parameter for the subduction signature in arc lavas. It is striking that, although water may be continuously released during subduction (e.g. Poli & Schmidt, 2002), arcs develop above a very distinct region of the subducting plate (around 80–120 km depth; England *et al.*, 2004). There appears to be minimum temperature in the mantle wedge above which melt is produced in preference to hydrous phases (chlorite, serpentine) when water enters the wedge (e.g. Grove *et al.*, 2009). Of all potential water-releasing reactions (e.g. Poli & Schmidt, 2002), serpentinite dehydration seems the most viable at sub-arc depths (e.g. Ulmer & Trommsdorff, 1995), adding large amounts of water but rather few trace elements (e.g. Scambelluri *et al.*, 2001). At 3 GPa, antigorite (~13 wt % H_2O) breaks down at ~700°C. Sediments at sub-arc depths will experience higher temperatures (>100°C) than the underlying serpentinites given their much closer proximity to the hot mantle wedge (e.g. Van Keken *et al.*, 2002). A slab-top temperature of ≥800°C accompanied by considerable amounts of excess water from the antigorite breakdown are in line with our proposal that monazite be (virtually) exhausted from the sedimentary portion of the slab. The role of serpentinites as major source for water beneath arcs (± interaction with sediments) has been highlighted many times in the literature (e.g. Hermann & Green, 2001; Bebout & Barton, 2002; Rüpke *et al.*, 2004; Arcay *et al.*, 2005; Stern *et al.*, 2006; Portnyagin *et al.*, 2007; Singer *et al.*, 2007; Spandler *et al.*, 2008). There is also independent evidence for dehydrating serpentinites beneath arcs from seismology and shear-wave splitting studies (e.g. Carlson, 2001; Seno *et al.*, 2001; Dobson *et al.*, 2002; Faccenda *et al.*, 2008; Burlini *et al.*, 2009). The presence of highly serpentinized mantle rocks is also confirmed from ocean drilling and dredging (e.g. Juteau *et al.*, 1990; Müntener & Manatschal, 2006), and can be estimated seismically (for more information, see, e.g. Hacker, 2008). We propose that serpentine breakdown, triggering 'flush melting' in the overlying subducted crust (basalt + sediment), is an important process in providing the slab-derived trace element signature beneath arcs. Even in arcs where serpentinite breakdown cannot be considered reasonable because of local thermal particularities, our conclusion that an external water source is required still holds for any arcs that show a 'sediment melt' geochemical signature. This is suggested by the fact that sediments, in a true

fluid-absent melting case, are nearly refractory up to relatively high slab-top temperatures.

ACKNOWLEDGEMENTS

We would like to thank R. Avanzinelli, A.-S. Bouvier, T. Elliott and T. Plank for very helpful discussions, all members of the Bristol Experimental Earth Studies (BEESt) group for stimulating discussions and help in the laboratory, S. Kearns for assistance with the microprobe (Bristol), C. Coath for assistance with the LA-ICP-MS (Bristol), and J. Craven and R. Hinton for assistance with the NERC ion-microprobe (Edinburgh) (project IMF 360/1008). The constructive reviews of T. Plank, an anonymous reviewer, and editor J. Hermann are gratefully acknowledged.

FUNDING

This work was supported by the Fonds National Suisse (PBLA2-119619 to S.S.) and by the Natural Environment Research Council (NE/G016615/1 to J.B.).

SUPPLEMENTARY DATA

Supplementary data for this paper are available at *Journal of Petrology* online.

REFERENCES

Aizawa, Y., Tatsumi, Y. & Yamada, H. (1999). Element transport by dehydration of subducted sediments. Implication for arc and ocean island magmatism. *Island Arc* **8**, 38–46.

Arcay, D., Tric, E. & Doin, M.-P. (2005). Numerical simulation of subduction zones. Effects of slab dehydration on the mantle wedge dynamics. *Physics of the Earth and Planetary Interiors* **149**, 133–153.

Auzanneau, E., Vielzeuf, D. & Schmidt, M. W. (2006). Experimental evidence of decompression melting during exhumation of subducted continental crust. *Contributions to Mineralogy and Petrology* **152**, 125–148.

Auzanneau, E., Schmidt, M. W., Vielzeuf, D. & Connolly, J. A. D. (2010). Titanium in phengite: a geobarometer for high temperature eclogites. *Contributions to Mineralogy and Petrology* **159**, 1–24.

Avanzinelli, R., Prytulak, J. & Elliott, T. (2008). Mantle melting beneath island arcs: U-series constraints from Marianas. *Geochimica et Cosmochimica Acta, Supplement* **72**, A37.

Ballevre, M., Pinardon, J.-L., Kienast, J.-R. & Vuichard, J.-P. (1989). Reversal of Fe–Mg partitioning between garnet and staurolite in eclogite-facies metapelites from the Champtoceaux Nappe (Brittany, France). *Journal of Petrology* **30**, 1321–1349.

Bebout, G. E. (2007). Trace elements and isotopic fluxes/subducted slabs. In: Holland, H. D. & Turekion, K. K. (eds) *Treatise on Geochemistry 3.20*. Oxford: Elsevier-Pergamon, pp. 1–50.

Bebout, G. E. & Barton, M. D. (2002). Tectonic and metasomatic mixing in a subduction-zone melange: insights into the geochemical evolution of the slab–mantle interface. *Chemical Geology* **187**, 79–106.

Berman, R. (1988). Internally-consistent thermodynamic data for minerals in the system Na_2O–K_2O–CaO–MgO–FeO–Fe_2O_3–Al_2O_3–SiO_2–TiO_2–H_2O–CO_2. *Journal of Petrology* **29**, 445–522.

Bishop, F. C., Smith, J. V. & Dawson, J. B. (1978). Na, K, P and Ti in garnet, pyroxene and olivine from peridotite and eclogite xenoliths from African kimberlites. *Lithos* **11**, 155–173.

Blundy, J. & Wood, B. (2003). Partitioning of trace elements between crystals and melts. *Earth and Planetary Science Letters* **210**, 383–397.

Blundy, J. D., Robinson, J. A. C. & Wood, B. J. (1998). Heavy REE are compatible in clinopyroxene on the spinel lherzolite solidus. *Earth and Planetary Science Letters* **160**, 493–504.

Bose, K. & Ganguly, J. (1995). Quartz–coesite transition revisited: reversed experimental determination at 500–1200°C and retrieved thermochemical properties. *American Mineralogist* **80**, 231–238.

Bouvier, A.-S., Metrich, N. & Deloule, E. (2008). Slab-derived fluids in the magma source of St. Vincent (Lesser Antilles Arc): volatile and light element imprints. *Journal of Petrology* **49**, 1427–1448.

Bowie, S. H. U. & Horne, J. E. T. (1953). Cheralite, a new mineral of the monazite group. *Mineralogical Magazine* **30**, 93–99.

Brenan, J. M., Shaw, H. F., Phinney, D. L. & Ryerson, F. J. (1994). Rutile–aqueous fluid partitioning of Nb, Ta, Hf, Zr, U and Th: implications for high field strength element depletions in island-arc basalts. *Earth and Planetary Science Letters* **128**, 327–339.

Bureau, H. & Keppler, H. (1999). Complete miscibility between silicate melts and hydrous fluids in the upper mantle: experimental evidence and geochemical implications. *Earth and Planetary Science Letters* **165**, 187–196.

Burlini, L., Di Toro, G. & Meredith, P. (2009). Seismic tremor in subduction zones: Rock physics evidence. *Geophysical Research Letters* **36**, L08305, doi:10.1029/2009GL037735.

Carlson, R. L. (2001). The abundance of ultramafic rocks in Atlantic Ocean crust. *Geophysical Journal International* **144**, 37–48.

Carlson, W. (2006). Rates of Fe, Mg, Mn, and Ca diffusion in garnet. *American Mineralogist* **91**, 1–11.

Castro, A. & Gerya, T. V. (2008). Magmatic implications mantle wedge plumes: Experimental study. *Lithos* **103**, 138–148.

Chakraborty, S. & Ganguly, J. (1991). Compositional zoning and cation diffusion in garnets. In: Ganguly, J. (ed.) *Diffusion, Atomic Ordering and Mass Transfer*. New York: Springer, pp. 120–175.

Class, C., Miller, D. M., Goldstein, S. L. & Langmuir, C. H. (2000). Distinguishing melt and fluid subduction and components in Umnak volcanics, Aleutian Arc. *Geochemistry, Geophysics, Geosystems* **1**, article number 1999GC000010.

Condomines, M. & Sigmarsson, O. (1993). Why are so many arc magmas close to ^{238}U–^{230}Th radioactive equilibrium? *Geochimica et Cosmochimica Acta* **57**, 4491–4497.

De Capitani, C. (1994). Gleichgewichts-Phasendiagramme: Theorie und Software. *Beihefte zum European Journal of Mineralogy* **72**, 48.

Dobson, D. P., Meredith, P. G. & Boon, S. A. (2002). Simulation of subduction zone seismicity by dehydration of serpentine. *Science* **298**, 1407–1410.

Domanik, K. J. & Holloway, J. R. (1996). The stability of phengitic muscovite and associated phases from 5·5 to 11 GPa: implications for deeply subducted sediments. *Geochimica et Cosmochimica Acta* **60**, 4133–4150.

Droop, G. (1987). A general equation for estimating Fe^{3+} concentrations in ferromagnesian silicates and oxides from microprobe analyses, using stochiometric criteria. *Mineralogical Magazine* **51**, 431–435.

Elliott, T. (2003). Tracers of the slab. In: Eiler, J. M. (ed.) *Inside the Subduction Factory. American Geophysical Union, Geophysical Monograph* **138**, 23–45.

Elliott, T., Plank, T., Zindler, A., White, W. & Bourdan, B. (1997). Element transport from slab to volcanic front at the Mariana arc. *Journal of Geophysical Research* **102**, 14991–15019.

England, P. & Wilkins, C. (2004). A simple analytical approximation to the temperature structure in subduction zones. *Geophysical Journal International* **159**, 1138–1154.

England, P., Engdahl, R. & Thatcher, W. (2004). Systematic variations in the depth of slabs beneath arc volcanoes. *Geophysical Journal International* **156**, 377–408.

Faccenda, M., Burlini, L., Gerya, T. V. & Mainprice, D. (2008). Fault-induced seismic anisotropy by hydration in subducting oceanic plates. *Nature* **455**, 1097–1100.

Foley, S. F., Barth, M. G. & Jenner, G. A. (2000). Rutile/melt partition coefficients for trace elements and assessment of the influence of rutile on the trace element characteristics of subduction zone magmas. *Geochimica and Cosmochimica Acta* **64**, 933–938.

Förster, H.-J. (1998). The chemical composition of REE–Y–Th–U-rich accessory minerals in peraluminous granites of the Erzgebirge–Fichtelgebirge region, Germany: Part I. The monazite–(Ce)-brabantite solid solution series. *American Mineralogist* **83**, 259–272.

Förster, H.-J. & Harlov, D. E. (1999). Monazite-(Ce)–huttonite solid solutions in granulite-facies metabasites from the Ivrea–Verbano Zone, Italy. *Mineralogical Magazine* **63**, 587–594.

Ganguly, J. (1972). Staurolite stability and related parageneses: Theory, experiments and applications. *Journal of Petrology* **13**, 335–365.

Ganguly, J., Tirone, M. & Hervig, R. (1998). Diffusion kinetics of samarium and neodymium in garnet, and a method for determining cooling rates of rocks. *Science* **281**, 805–807.

Green, T. H., Blundy, J. D., Adam, J. & Yaxley, G. M. (2000). SIMS determination of trace element partition coefficients between garnet, clinopyroxene and hydrous basaltic liquids at 2–7·5 GPa and 1080–1200°C. *Lithos* **53**, 165–187.

Grove, T. L., Parman, S. W., Bowring, S. A., Price, R. C. & Baker, M. B. (2002). The role of an H_2O-rich fluid component in the generation of primitive basaltic andesites and andesites from the Mt. Shasta region, N California. *Contributions to Mineralogy and Petrology* **142**, 375–396.

Grove, T. L., Till, C. B., Lev, E., Chatterjee, N. & Medard, E. (2009). Kinematic variables and water transport control the formation and location of arc volcanoes. *Nature* **459**, 694–697.

Hacker, B. R. (2006). Pressure and temperature of ultrahigh-pressure metamorphism: Implications for UHP tectonics and H_2O in subducting slabs. *International Geology Review* **48**, 1053–1066.

Hacker, B. R. (2008). H_2O subduction beyond arcs. *Geochemistry, Geophysics, Geosystems* **9**, doi:10.1029/2007GC001707.

Haggerty, S. E., Fung, A. T. & Burt, D. M. (1994). Apatite, phosphorus and titanium in eclogitic garnet from the upper mantle. *Geophysical Research Letters* **21**, 1699–1702.

Hanson, G. N. & Langmuir, C. H. (1978). Modelling of major elements in mantle–melt systems using trace element approaches. *Geochimica et Cosmochimica Acta* **42**, 725–741.

Hawkesworth, C. J., Gallagher, K., Hergt, J. M. & McDermott, F. (1993). Mantle and slab contributions in arc magmas. *Annual Review of Earth and Planetary Sciences* **21**, 175–204.

Hellman, P. L. & Green, T. H. (1979). High-pressure experimental crystallization of staurolite in hydrous mafic compositions. *Contributions to Mineralogy and Petrology* **68**, 369–372.

Hermann, J. (2002). Allanite: thorium and light rare earth element carrier in subducted crust. *Chemical Geology* **192**, 289–306.

Hermann, J. & Green, D. H. (2001). Experimental constraints on high pressure melting in subducted crust. *Earth and Planetary Science Letters* **188**, 149–168.

Hermann, J. & Rubatto, D. (2009). Accessory phase control on the trace element signature of sediment melts in subduction zone. *Chemical Geology* **265**, 512–526.

Hermann, J. & Spandler, C. J. (2008). Sediment melts at sub-arc depths: An experimental study. *Journal of Petrology* **49**, 717–740.

Hermann, J., Spandler, C., Hack, A. & Korsakov, A. V. (2006). Aqueous fluids and hydrous melts in high-pressure and ultra-high-pressure rocks: Implications for element transfer in subduction zones. *Lithos* **92**, 399–417.

Hinton, R. W. (1990). Ion microprobe trace-element analysis of silicates: Measurements of multi-element glasses. *Chemical Geology* **83**, 11–25.

Holland, T. & Powell, R. (1998). Internally consistent thermodynamic data set for phases of petrological interest. *Journal of Metamorphic Geology* **16**, 309–343.

Huang, W. L. & Wyllie, P. J. (1973). Melting relations of muscovite-granite to 35 kbar as a model for fusion of metamorphosed subducted oceanic sediments. *Contributions to Mineralogy and Petrology* **42**, 1–14.

Huang, W. L. & Wyllie, P. J. (1981). Phase relations of S-type granite with H_2O to 35 kbar: muscovite granite from Harney Peak, South Dakota. *Journal of Geophysical Research* **86**, 10515–10529.

Janots, E., Brunet, F., Goffe, B., Poinssot, C., Burchard, M. & Cemic, L. (2007). Thermochemistry of monazite-(La) and dissakisite-(La): implications for monazite and allanite stability in metapelites. *Contributions to Mineralogy and Petrology* **154**, 1–14.

Johnson, M. C. & Plank, T. (1999). Dehydration and melting experiments constrain the fate of subducted sediments. *Geochemistry, Geophysics, Geosystems* **1**, article number 1999GC000014.

Juteau, T., Cannat, M. & Lagabrielle, Y. (1990). Serpentinized peridotites in the upper oceanic crust away from transform zones: A comparison of the results of previous DSDP and ODP legs. In: Detrick, R., Honnorez, J., Bryan, W. B. & Juteau, T. *et al*. (eds) *Proceedings of the Ocean Drilling Program, Scientific Results, 106/109*. College Station, TX: Ocean Drilling Program, pp. 303–308.

Keller, L. M., De Capitani, C. & Abart, R. (2005). A quaternary solution model for white micas based on natural coexisting phengite–paragonite pairs. *Journal of Petrology* **46**, doi:10.1093/petrology/egi050.

Kessel, R., Schmidt, M. W., Ulmer, P. & Pettke, T. (2005*a*). Trace element signature of subduction zone fluids, melts and supercritical liquids at 120–180 km depth. *Nature* **437**, 724–727.

Kessel, R., Ulmer, P., Pettke, T., Schmidt, M. W. & Thompson, A. B. (2005*b*). The water–basalt system at 4 to 6 GPa: Phase relations and second critical endpoint in a K-free eclogite at 700 to 1400°C. *Earth and Planetary Science Letters* **237**, 873–892.

Klemme, S., Blundy, J. D. & Wood, B. J. (2002). Experimental constraints on major and trace element partitioning during partial melting of eclogite. *Geochimica and Cosmochimica Acta* **66**, 3109–3123.

Klemme, S., Prowatke, S., Hametner, K. & Günther, D. (2005). Partitioning of trace elements between rutile and silicate melts: Implications for subduction zones. *Geochimica and Cosmochimica Acta* **69**, 2361–2371.

Klimm, K., Blundy, J. D. & Green, T. H. (2008). Trace element partitioning and accessory phase saturation during H_2O-saturated melting of basalt with implications for subduction zone chemical fluids. *Journal of Petrology* **49**, 523–553.

Krenn, E., Janak, M., Finger, F., Broska, I. & Konecny, P. (2009). Two types of metamorphic monazite with contrasting La/Nd, Th, and Y signatures in an ultrahigh-pressure metapelite from the Pohorje Mountains, Slovenia: Indications for pressure-dependent REE exchange between apatite and monazite? *American Mineralogist* **94**, 801–815.

Kress, V. C. & Carmichael, I. S. E. (1991). The compressibility of silicate liquids containing Fe_2O_3 and the effect of composition,

temperature, oxygen fugacity and pressure on their redox states. *Contributions to Mineralogy and Petrology* **108**, 82–92.

Leake, B., Woolley, A., Arps, C., Birch, W., Gilbert, M., Grice, J., Hawthorne, F., Kato, A., Kisch, H., Krivovichev, V., Linthout, K., Laird, J., Mandarino, J., Maresch, W., Nickel, E., Rock, N., Schumacher, J., Smith, D., Stephenson, N., Ungaretti, L., Whittaker, E. & Guo, Y. (1997). Nomenclature of amphiboles: Report of the subcommittee on amphiboles of the International Mineralogical Association, commission on new minerals and mineral names. *American Mineralogist* **82**, 1019–1037.

Manning, C. E. (2004). The chemistry of subduction zone fluids. *Earth and Planetary Science Letters* **223**, 1–16.

McCulloch, M. T. & Gamble, J. A. (1991). Geochemical and geodynamical constraints on subduction zone magmatism. *Earth and Planetary Science Letters* **102**, 358–374.

McDade, P., Wood, B. J., van Westrenen, W., Brooker, R., Gudmundsson, G., Soulard, H., Najorka, J. & Blundy, J. (2002). Pressure corrections for a selection of piston-cylinder cell assemblies. *Mineralogical Magazine* **66**, 1021–1028.

McDermott, F. M. & Hawkesworth, C. (1991). Th, Pb, and Sr isotope variations in young island arc volcanics and oceanic sediments. *Earth and Planetary Science Letters* **104**, 1–15.

Melzer, S. & Wunder, B. (2000). Island-arc basalt alkali ratios: constraints from phengite–fluid partitioning experiments. *Geology* **28**, 583–586.

Montel, J.-M. (1993). A model for monazite/melt equilibrium and application to the generation of granitic magmas. *Chemical Geology* **110**, 127–146.

Morimoto, N., Fabries, J., Ferguson, A. K., Ginzburg, I. V., Ross, M., Seifert, F. A., Zussman, J., Aoki, K. & Gottardi, G. (1988). Nomenclature of pyroxenes. *American Mineralogist* **73**, 1123–1133.

Müntener, O. & Manatschal, G. (2006). High degrees of melt extraction recorded by spinel harzburgite of the Newfoundland margin: the role of inheritance and consequences for the evolution of the southern North Atlantic. *Earth and Planetary Science Letters* **252**, 437–452.

Nichols, G. T., Wyllie, P. J. & Stern, C. R. (1994). Subduction zone melting of pelagic sediments constrained by melting experiments. *Nature* **371**, 785–788.

Nichols, G. T., Wyllie, P. J. & Stern, C. R. (1996). Experimental melting of pelagic sediment, constraints relevant to subduction. In: Bebout, G. E., Scholl, D. H., Kirby, S. P. & Platt, J. (eds) *Subduction: Top to Bottom. American Geophysical Union, Geophysical Monograph* **96**, 293–298.

Pawley, A. R. & Holloway, J. R. (1993). Water sources for subduction zone volcanism—new experimental constraints. *Science* **260**, 664–667.

Pearce, J. A. & Cann, J. R. (1973). Tectonic setting of basic volcanic rocks determined using trace element analysis. *Earth and Planetary Science Letters* **19**, 290–300.

Pertermann, M., Hirschmann, M. M., Hametner, K., Gunther, D. & Schmidt, M. W. (2004). Experimental determination of trace element partitioning between garnet and silica-rich liquid during anhydrous partial melting of MORB-like eclogite. *Geochemistry, Geophysics, Geosystems* **5**, Q05A01, doi:10.1029/2003GC000638.

Pichavant, M., Valencia Herrera, J., Boulmier, S., Briqueu, L., Joron, J. L., Juteau, M., Marin, L., Michard, A., Sheppard, S. M. F., Treuil, M. & Venet, M. (1987). The Macusani glasses, SE Peru: evidence of chemical fractionation in peraluminous magmas. In: Mysen, B. O. (ed.) *Magmatic Processes: Physicochemical Principles. Geochemical Society Special Publications* **1**, 359–373.

Plank, T. (2005). Constraints from thorium/lanthanum on sediment recycling at subduction zones and the evolution of the continents. *Journal of Petrology* **46**, 921–944.

Plank, T. & Langmuir, C. H. (1993). Tracing trace element from sediment input to volcanic output at subduction zones. *Nature* **362**, 799–742.

Plank, T. & Langmuir, C. H. (1998). The chemical composition of subducting sediment and its consequences for the crust and mantle. *Chemical Geology* **145**, 325–394.

Poli, S. & Schmidt, M. W. (2002). Petrology of subducted slabs. *Annual Review of Earth and Planetary Sciences* **30**, 207–235.

Portnyagin, M., Hoernle, K., Plechov, P., Mironov, N. & Khubunaya, S. (2007). Constraints on mantle melting and composition and nature of slab components in volcanic arcs from volatiles (H_2O, S, Cl, F) and trace elements in melt inclusions from the Kamchatka Arc. *Earth and Planetary Science Letters* **255**, 53–69.

Rapp, R. P. & Watson, E. B. (1986). Monazite solubility and dissolution kinetics: implications for the thorium and light rare earth chemistry of felsic magmas. *Contributions to Mineralogy and Petrology* **94**, 304–316.

Richardson, S. W. (1968). Staurolite stability in a part of the system Fe–Al–Si–O–H. *Journal of Petrology* **9**, 467–488.

Rubatto, D. & Hermann, J. (2007). Experimental zircon/melt and zircon/garnet trace element partitioning and implications for the geochronology of crustal rocks. *Chemical Geology* **241**, 38–61.

Rüpke, L. H., Phipps-Morgan, J., Hort, M. & Connolly, J. (2004). Serpentine and the subduction water cycle. *Earth and Planetary Science Letters* **223**, 17–34.

Ryerson, F. J. & Watson, E. B. (1987). Rutile saturation in magmas—implications for Ti–Nb–Ta depletion in island-arc basalts. *Earth and Planetary Science Letters* **86**, 225–239.

Scambelluri, M., Rampone, E. & Piccardo, G. B. (2001). Fluid and element cycling in subducted serpentinite: a trace element study of the Erro–Tobbio high-pressure ultramafites (western Alps NW Italy). *Journal of Petrology* **42**, 55–67.

Schmidt, M. W. (1996). Experimental constraints on recycling of potassium from subducted oceanic crust. *Science* **272**, 1927–1930.

Schmidt, M. W., Dardon, A., Chazot, G. & Vannucci, R. (2004*a*). The dependence of Nb and Ta rutile–melt partitioning on melt composition and Nb/Ta fractionation during subduction processes. *Earth and Planetary Science Letters* **226**, 415–432.

Schmidt, M. W., Vielzeuf, D. & Auzanneau, E. (2004*b*). Melting and dissolution of subducting crust at high pressures: the key role of white mica. *Earth and Planetary Science Letters* **228**, 65–84.

Seno, T., Zhao, D., Kobayashi, Y. & Nakamura, M. (2001). Dehydration of serpentinized slab mantle: Seismic evidence from southwest Japan. *Earth, Planets, and Space* **53**, 861–871.

Singer, B. S., Jicha, B. R., Leeman, W. P., Rogers, N. W., Thirlwall, M. F., Ryan, J. & Nicolaysen, K. E. (2007). Along-strike trace element and isotopic variation in Aleutian Island arc basalt: Subduction melts sediments and dehydrates serpentine. *Journal of Geophysical Research* **112**, B06206, doi:10.1029/2006JB004897.

Sorensen, S. S., Grossman, J. N. & Perfit, M. R. (1997). Phengite-hosted LILE enrichment in eclogite and related rocks; implications for fluid-mediated mass transfer in subduction zones and arc magma genesis. *Journal of Petrology* **38**, 3–34.

Spandler, C., Hermann, J., Arculus, R. & Mavrogenes, J. (2003). Redistribution of trace elements during prograde metamorphism from lawsonite blueschist to eclogite facies; implications for deep subduction zone processes. *Contributions to Mineralogy and Petrology* **146**, 205–222.

Spandler, C., Hermann, J., Faure, K., Mavrogenes, J. A. & Arculus, R. J. (2008). The importance of talc and chlorite 'hybrid'

rocks for volatile recycling through subduction zones; evidence from the high-pressure subduction mélange of New Caledonia. *Contributions to Mineralogy and Petrology* **155**, 181–198.

Spear, F. S. & Pyle, J. M. (2002). Apatite, monazite, and xenotime in metamorphic rocks. In: Kohn, M. L., Rakovan, J. & Hughes, J. M. (eds) *Phosphates—Geochemical, Geobiological and Materials Importance. Mineralogical Society of America and Geochemical Society, Reviews in Mineralogy and Geochemistry* **48**, 293–335.

Stalder, R., Foley, S. F., Brey, G. P. & Horn, I. (1998). Mineral–aqueous fluid partitioning of trace elements at 900–1200°C an 3·0–5·7 GPa: new experimental data for garnet, clinopyroxene, and rutile, and implications for mantle metasomatism. *Geochimica et Cosmochimica Acta* **62**, 1781–1801.

Stern, R. J., Kohut, E., Bloomer, S. H., Leybourne, M., Fouch, M. & Vervoort, J. (2006). Subduction factory processes beneath the Guguan cross-chain, Mariana Arc: No role for sediments, are serpentinites important? *Contributions to Mineralogy and Petrology* **151**, 202–221.

Tatsumi, Y. & Kogiso, T. (1997). Trace element transport during dehydration processes in the subducted oceanic crust: 2. Origin of chemical and physical characteristics in arc magmatism. *Earth and Planetary Science Letters* **148**, 207–221.

Tera, F., Brown, L., Morris, J., Sacks, I. S., Klein, J. & Middleton, R. (1986). Sediment incorporation in island arc magmas: inferences from ^{10}Be. *Geochimica et Cosmochimica Acta* **50**, 636–660.

Thirlwall, M. F., Smith, T. E., Graham, A. M., Theodorou, N., Hollings, P., Davidson, J. P. & Arculus, R. J. (1994). High field strength element anomalies in arc lavas: source or process? *Journal of Petrology* **35**, 819–838.

Thomsen, T. B. & Schmidt, M. W. (2008*a*). Melting of carbonated pelites at 2·5–5·0 GPa, silicate–carbonate liquid immiscibility, and potassium–carbon metasomatism of the mantle. *Earth and Planetary Science Letters* **267**, 17–31.

Thomsen, T. B. & Schmidt, M. W. (2008*b*). The biotite to phengite reaction and mica-dominated melting in fluid + carbonate-saturated pelites at high pressures. *Journal of Petrology* **49**, 1889–1914.

Tirone, M., Ganguly, J., Dohmen, R., Langenhorst, F., Hervig, R. & Becker, H. (2005). Rare earth diffusion kinetics in garnet: Experimental studies and applications. *Geochimica et Cosmochimica Acta* **69**, 2385–2398.

Townsend, K. J., Miller, C. F., D'Andrea, J. L., Ayers, J. C., Harrison, T. M. & Coath, C. D. (2000). Low temperature replacement of monazite in the Ireteba granite, Southern Nevada: geochronological implications. *Chemical Geology* **172**, 95–112.

Ulmer, P. & Trommsdorff, V. (1995). Serpentine stability to mantle depths and subduction-related magmatism. *Science* **268**, 858–861.

van Keken, P. E., Kiefer, B. & Peacock, S. M. (2002). High-resolution models of subduction zones: implications for mineral dehydration reactions and the transport of water into the deep mantle. *Geochemistry, Geophysics, Geosystems* **3**, doi:10.1029/2001GC000256.

van Orman, J., Grove, T., Shimizu, N. & Layne, G. (2002). Rare earth element diffusion in a natural pyrope single crystal at 2·8 GPa. *Contributions to Mineralogy and Petrology* **142**, 416–424.

van Westrenen, W., Blundy, J. & Wood, B. (1999). Crystal-chemical controls on trace element partitioning between garnet and anhydrous silicate melt. *American Mineralogist* **84**, 838–847.

van Westrenen, W., Wood, B. J. & Blundy, J. D. (2001). A predictive thermodynamic model of garnet–melt trace element partitioning. *Contributions to Mineralogy and Petrology* **142**, 219–234.

Watson, E. B. & Harrison, M. T. (1983). Zircon saturation revisited: temperature and composition effects in a variety of crustal magma types. *Earth and Planetary Science Letters* **64**, 295–304.

Williams, M. L., Jercinovic, M. J. & Hetherington, C. J. (2007). Microprobe monazite geochronology: understanding geologic processes by integrating composition and chronology. *Annual Review of Earth and Planetary Sciences* **35**, 137–175.

Wolf, M. B. & London, D. (1995). Incongruent dissolution of REE- and Sr-rich apatite in peraluminous granitic liquids. Differential apatite, monazite, and xenotime solubilities during anatexis. *American Mineralogist* **80**, 765–775.

Wood, B. J., Blundy, J. D. & Robinson, J. A. C. (1999). The role of clinopyroxene in generating U-series disequilibrium during mantle melting. *Geochimica et Cosmochimica Acta* **63**, 1613–1620.

Wunder, B. & Melzer, S. (2003). Experimental evidence on phlogopite mantle metasomatism induced by phengite dehydration. *European Journal of Mineralogy* **15**, 641–647.

Xiong, X., Keppler, H., Audetat, A., Gudfinnsson, G., Sun, W., Song, M., Xiao, W. & Yuan, L. (2009). Experimental constraints on rutile saturation during partial melting of metabasalt at the amphibolite to eclogite transition, with application to TTG genesis. *American Mineralogist* **94**, 1175–1186.

Yang, P. S. & Pattison, D. (2006). Genesis of monazite and Y zoning in garnet from the Black Hills, South Dakota. *Lithos* **88**, 233–253.

Zack, T., Rivers, T. & Foley, S. (2001). Cs–Rb–Ba systematics in phengite and amphibole: an assessment of fluid mobility at 2·0 GPa in eclogites from Trescolmen. *Contributions to Mineralogy and Petrology* **140**, 651–669.

Zack, T., Kronz, A., Foley, S. & Rivers, T. (2002). Trace element abundance in rutiles from eclogites and associated garnet mica schists. *Chemical Geology* **184**, 97–122.

Zhu, X. K. & O'Nions, R. K. (1999). Zonation of monazite in metamorphic rocks and its implications for high temperature thermochronology: a case study from the Lewisian Terrain. *Earth and Planetary Science Letters* **171**, 209–220.